

A Closer Look into Slickensides: Deformation On and Under Fault Surfaces

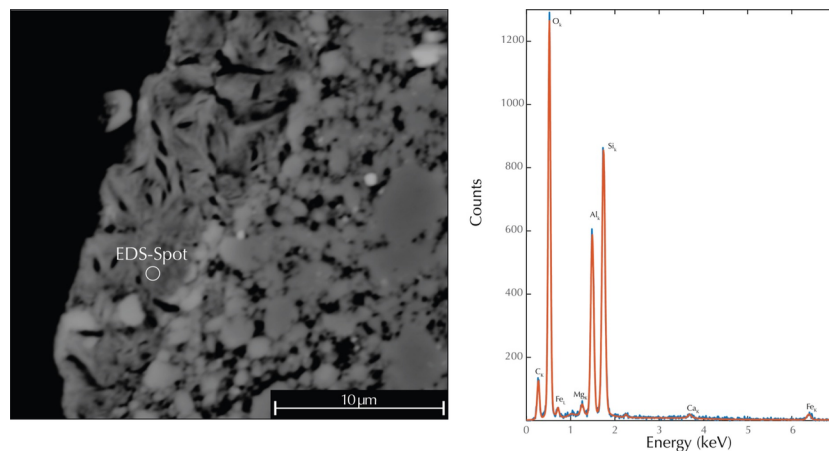
Daniel Ortega-Arroyo¹ and Matej Pec¹

¹Massachusetts Institute of Technology

November 21, 2022

Abstract

Accurate descriptions of natural fault surfaces and associated fault rocks are important for understanding fault zone processes and properties. Slickensides—grooved polished surfaces that record displacement and wear along faults—develop measurable roughness and characteristic microstructures during fault slip. We quantify the roughness of natural slickensides from three different fault surfaces by calculating the surfaces power spectra and height distributions and analyze the microstructures formed above and below the slickensides. Slickenside surfaces exhibit anisotropic self-affine roughness with corresponding mean Hurst exponents in directions parallel— 0.53 ± 0.07 — and perpendicular— -0.6 ± 0.1 — to slip, consistent with reports from other fault surfaces. Additionally, surfaces exhibit non-Gaussian height distributions, with their skewness and kurtosis roughness parameters having noticeable dependence on the scale of observation. Below the surface, microstructural analyses reveal that S-C-C' fabrics develop adjacent to a C-plane-parallel principal slip zone characterized by a sharp decrease in clast size and a thin ($\approx 100 \mu\text{m}$) nanoparticulate-rich principal slip surface (PSS). These microstructures are present in most analyzed samples suggesting they commonly form during slickenside development regardless of lithology or tectonic setting. Our results suggest that 1) PSS likely arise by progressive localization along weaker oriented fabrics 2) deformation along PSS's is energetic enough to comminute the rocks into nanometric grains, and 3) fault geometry can be further characterized by studying the height distributions of fault surfaces, which are likely to impact stress distributions and frictional responses along faults.



1 **A Closer Look into Slickensides: Deformation On and Under Fault Surfaces**

2 **Daniel Ortega-Arroyo & Matej Pec**

3 Department of Earth, Atmospheric, and Planetary Sciences, Massachusetts Institute of
4 Technology, Cambridge, Massachusetts, 02139, USA

5

6 Corresponding author: Daniel Ortega-Arroyo (dortega@mit.edu)

7

8 **Key Points:**

- 9 · Fault surfaces exhibit a non-Gaussian self-affine roughness with scale-dependent
- 10 skewness and kurtosis.
- 11 · Progressive localization of strain along oriented fabrics give rise to slickenside structures
- 12 · Nanoparticulate layers are common on fault rocks regardless of lithology or tectonic
- 13 setting

14

15

16 **Key Words:** fault mirror, slickenside, fault surface roughness, principal slip zone,
17 nanograins

18

19

20

21

22 **Abstract**

23 Accurate descriptions of natural fault surfaces and associated fault rocks are important for
24 understanding fault zone processes and properties. Slickensides--grooved polished surfaces that
25 record displacement and wear along faults-- develop measurable roughness and characteristic
26 microstructures during fault slip. We quantify the roughness of natural slickensides from three
27 different fault surfaces by calculating the surfaces power spectra and height distributions and
28 analyze the microstructures formed above and below the slickensides. Slickenside surfaces exhibit
29 anisotropic self-affine roughness with corresponding mean Hurst exponents in directions parallel-
30 - 0.53 ± 0.07 -- and perpendicular -- 0.6 ± 0.1 -- to slip, consistent with reports from other fault
31 surfaces. Additionally, surfaces exhibit non-Gaussian height distributions, with their skewness and
32 kurtosis roughness parameters having noticeable dependence on the scale of observation. Below
33 the surface, microstructural analyses reveal that S-C-C' fabrics develop adjacent to a C-plane-
34 parallel principal slip zone characterized by a sharp decrease in clast size and a thin ($\leq 100 \mu\text{m}$)
35 nanoparticulate-rich principal slip surface (PSS). These microstructures are present in most
36 analyzed samples suggesting they commonly form during slickenside development regardless of
37 lithology or tectonic setting. Our results suggests that 1) PSS likely arise by progressive
38 localization along weaker oriented fabrics 2) deformation along PSS's is energetic enough to
39 comminute the rocks into nanometric grains, and 3) fault geometry can be further characterized by
40 studying the height distributions of fault surfaces, which are likely to impact stress distributions
41 and frictional responses along faults.

42

43 **Plain Language Summary**

44 Grooved, polished rock surfaces known as slickensides are associated with wear along faults,
45 which makes them useful indicators of the kinematics and grain-scale processes occurring during
46 fault slip. We study naturally formed slickensides from three different faults with different rock
47 compositions. Slickenside surfaces reveal directionally dependent textures with respect to the
48 grooves that exhibit similar patterns over a wide range of length scales, as many other faults do.
49 The slickenside heights, however, do not follow a normal distribution, and the shape of the
50 distributions varies with the scale of observation.

51

52 Microscopic observations below the surface show that oriented patterns form next to the
53 slickenside surface with most of the deformation concentrated within a narrow region ($\leq 100 \mu\text{m}$)
54 near the surface. This region is mostly composed of ultra-fine particles ($\leq 1 \mu\text{m}$) and other
55 frictionally produced films. Our results suggest that 1) such fault surfaces emerge through
56 progressive deformation along ever weakening regions and 2) faults can release enough energy to
57 break the rocks into nano-sized particles during slip. Further, our results highlight additional
58 geometrical information of the surface which can impact how stress is distributed along faults and
59 consequently how faults slip.

60 **1. Introduction**

61 Geologic observations indicate that slickensides—smooth, striated rock surfaces-- and
62 associated fault rocks record motion and mechanical wear between faulted blocks (e.g. Doblas,
63 1998; Fleuty, 1975; Lyell, 1871; Petit, 1987). The direct imprint of wear recorded along
64 slickensides makes them particularly useful kinematic indicators as well as indicators of the grain
65 scale processes leading to- and occurring during-slip. Studies on natural and experimental fault
66 surfaces have suggested a wide range of processes can be recorded within slickensides and
67 associated fault rocks such as: mechanical amorphization and silica gel formation (Houser et al.,
68 2021; Kirkpatrick et al., 2013; Ohl et al., 2020; Pec et al., 2012, 2016; Rowe et al., 2019; Taylor
69 et al., 2021; Toy et al., 2017), extreme comminution and nanoparticle formation (Di Toro et al.,
70 2011; Houser et al., 2021; Kuo et al., 2016; Ohl et al., 2020; Power & Tullis, 1989; Siman-Tov et
71 al., 2013; Sun & Pec, 2021; Tisato et al., 2012; Toy et al., 2017; Verberne et al., 2014, 2019; Viti
72 et al., 2016), localized frictionally induced heating (Ault et al., 2019; Evans et al., 2014; Houser et
73 al., 2021; Ohl et al., 2020; Rowe et al., 2019; Siman-Tov et al., 2015; Taylor et al., 2021; Toy et
74 al., 2017; Verberne et al., 2014), frictional melting (Magloughlin & Spray, 1992; Nielsen et al.,
75 2010; Spray, 1989, 1992), crystal-plastic deformation (Bestmann et al., 2011; J. Chen et al., 2020;
76 Ohl et al., 2020), rupture propagation direction (Kearse et al., 2019; Macklin et al., 2021) and
77 temporal changes in coseismic slip (Otsubo et al., 2013), highlighting their potential usefulness for
78 deciphering the physico-chemical processes that occur during fault slip. Such observations are
79 crucial for the understanding of the microphysical origins of friction and could eventually lead to
80 constraining microstructural fingerprints associated with high slip velocities, which remains one
81 of the outstanding questions in the study of fault zones (Rowe & Griffith, 2015).

82 Slickensides further allow us to study and characterize in detail and over many scales the
83 geometry of single fault segments (Bistacchi et al., 2011; Brodsky et al., 2016; Candela et al.,
84 2009, 2012; J.-J. Lee & Bruhn, 1996; Power et al., 1987). This is particularly important as fault
85 geometry has been shown to be a major factor contributing to earthquake rupture nucleation,
86 propagation and arrest (e.g., Ben-Zion & Rice, 1997; Cattania & Segall, 2021; Sagy &
87 Lyakhovskiy, 2019; Scholz, 2019; Tal et al., 2020). The irregularities on the surface geometry,
88 known as roughness, exert a direct control on surface properties that control surface interactions
89 such as real area of contact, friction, wear, and lubrication (e.g., Bhushan, 2013; Boneh & Reches,
90 2018; Bowden et al., 1939; Dieterich & Kilgore, 1996; Tal et al., 2020).

91 Over the last decades, studies have shown that fault roughness exhibits a self-affine
92 geometry that spans many scales of observation (Bistacchi et al., 2011; Brodsky et al., 2016; S. R.
93 Brown & Scholz, 1985; Candela et al., 2009, 2012; X. Chen et al., 2013; Kirkpatrick & Brodsky,
94 2014; J.-J. Lee & Bruhn, 1996; Power et al., 1987; Shervais & Kirkpatrick, 2016; Siman-Tov et
95 al., 2015; Toy et al., 2017). In contrast to a self-similar geometry that is scale independent, a self-
96 affine fractal is scale dependent. This means that in order to observe self-similarity, i.e., scale-
97 invariance, an affine transformation that scales the axes of the fractal surface (e.g., length vs.
98 width) differently is needed (Mandelbrot, 1985). Due to current limitations of subsurface imaging
99 techniques, most of our understanding of fault processes relies on the study of exhumed fault
100 surfaces, experiments, and numerical models.

101 Current fault zone models feature a zone of distributed fracturing with increasing intensity
102 that culminates in a highly strained fault core characterized by an abundance of highly fractured
103 and comminuted fault rocks (Caine et al., 1996; F. M. Chester & Logan, 1986; Faulkner et al.,
104 2010). The architecture of fault zones is then generally described by: a) distribution and number

105 of cores, b) width and intensity of fracturing within the damage zone, and c) distribution of
106 subsidiary faults (Faulkner et al., 2010, 2011). Fault zones that are currently exposed experienced
107 a number of discrete slip events that ultimately lead to fault zone development (e.g., Gold et al.,
108 2020; Shervais & Kirkpatrick, 2016). Slickensides can form between two shearing blocks and
109 subsequently form prominent fault surfaces. The architecture of a fault zone, structures found
110 within fault zones, and the strain partitioning between them, need to be known so that their
111 potential effect on ground motion can be evaluated. Rupture models typically rely on the
112 interaction of one or few rough fault segments (e.g., Bruhat et al., 2020; Cattania & Segall, 2021;
113 Graves & Pitarka, 2016; Ulrich et al., 2019) with recently developed models accounting for a much
114 larger number of interacting slip surfaces (Chu et al., 2021; Tsai et al., 2021; Tsai & Hirth, 2020).

115 Thus, this work aims to thoroughly describe the geometry of discrete slip surfaces and
116 identify the dominant deformation mechanisms occurring during slip and slickenside
117 development. We examine the surface and associated microstructures of individual principal slip
118 structures recorded along natural slickensides from three different fault systems hosted within
119 different lithologies. We start by studying the roughness of each slickenside using Fourier Power
120 Spectrum Density analyses (PSD) to derive their respective Hurst exponent, otherwise known as
121 the roughness coefficient. The geometry of the different slip surfaces is further characterized by
122 statistically describing the height distributions of the surfaces at multiple scales of observation.
123 Our work on slickensides is then extended beyond the surface to the fault rocks that host them by
124 conducting detailed microstructural and grain size distribution analyses of the rock volume
125 surrounding the fault surface. Lastly, we discuss the implications of our observation on our
126 understanding of fault processes

127

128 **2 Methods**

129 We focused on slickenside surfaces collected from 3 different fault systems--a strike slip
130 Plan de los Plátanos fault (PP) in SE Jalisco, Mexico, the Big Piute Ranges low angle normal fault
131 (BP), and Waterman Hills detachment fault (WH), both in SE California-- that represent different
132 lithologies and/or tectonic settings as summarized in Fig. 1. At each locality, we aimed to sample
133 specimens that preserved both sides of the fault surface, if possible, to better capture the structures
134 and materials that comprise slickensides. The faults--PP, BP, and WH-- cut through primarily
135 andesite, quartzite, and mylonitic metasedimentary (*MMS*) rocks, respectively.

136

137 **2.1 Brief Geologic Background of Analyzed Samples**

138 **2.1.1 Plan de los Plátanos Fault**

139 The Plan de los Plátanos is right lateral strike slip fault that accommodates ~430 m of
140 displacement. It is located NW of Autlán de Navarro, Jalisco, Mexico within the Jalisco Block, a
141 rigid tectonic block developed during the Miocene that moves independently from the Rivera and
142 North American plates bounded by the Tepic-Zacoalco Rift and the Colima Rift (De la Teja Segura
143 & Roque Ayala, 2007; Ferrari et al., 2000; Rosas-Elguera et al., 1996). The PP fault is a subvertical
144 structure that cuts through Laramide-folded Tertiary andesite-rhyolite tuffs that overlain the
145 Tepaltepec cretaceous volcano-sedimentary sequence, intruded by the late Cretaceous- early
146 Paleogene Tomatlan granitic batholith (De la Teja Segura & Roque Ayala, 2007).

147 The PP slickenside sample was collected from a minor splay exposed on the side of the road near
148 the town of Jalocote (De la Teja Segura & Roque Ayala, 2007). The sample records multiple
149 slickenside surfaces hosted in a porphyritic andesite with sericitized plagioclase phenocrysts in the
150 0.1-1.0 mm range. The rock is hydrothermally altered with secondary chlorite and iron oxides

151 comprising the bulk of the fracture fill along with few quartz-rich veins. Despite the heavy
152 alteration and hosting of slickensides, the host rock seldom records pervasive/distributed
153 deformation as the primary igneous texture is relatively intact a few cm away from the slip surface.

154

155 **2.1.2 Big Piute Normal Fault**

156 The Big Piute Mountains lie in the eastern Mojave Desert within a late Cretaceous ductile
157 deformation belt of synkinematic metamorphism and granitoid pluton emplacement. Thick-
158 skinned thrusting places Proterozoic crystalline basement over recumbently folded Paleozoic
159 meta-sediments. A sequence of Tertiary sedimentary and volcanic rocks overlies Mesozoic,
160 Paleozoic and Proterozoic rocks. Tertiary faults cut through all strata and account for 20-30%
161 crustal extension accommodated in the region (Fletcher & Karlstrom, 1990).

162 Slickensides from this location were collected from small subsidiary faults within the damage zone
163 of the BP that likely accommodated no more than a few meters of displacement. Unlike the other
164 samples, the slickenside in these faults are hosted within a monomineralic quartzite host rock with
165 a primary grain size ranging from 200 μm - 1 mm.

166

167 **2.1.3 Waterman Hills Fault**

168 The Waterman Hill Detachment Fault (WHDF) is a low angle detachment fault thought to
169 accommodate more than 40 km of total slip located within Central Mojave Metamorphic Core
170 Complex exposed along the Mitchell Range N of Barstow, SE California (Glazner et al., 1989).
171 The WHDF juxtaposes Tertiary sedimentary and volcanic strata against Mesozoic granodiorites
172 and the Waterman Gneiss comprised by mylonitized late Proterozoic to Paleozoic
173 metasedimentary and metaigneous lithologies (Fletcher et al., 1999; Glazner et al., 1989).

174

175 The samples were collected from a minor fault exposure found within the mylonitic
176 footwall of the WHDF. The fault surface occurs at the lithological boundary of metaigneous,
177 quartzitic and metacarbonate protoliths. The slickensides are hosted within a thick cataclasite
178 (larger than the hand samples) comprising multiple lithologies. The rock itself is overprinted by
179 hydrothermal alteration and calcite-filled fractures.

180

181 **2.2 Sample Preparation**

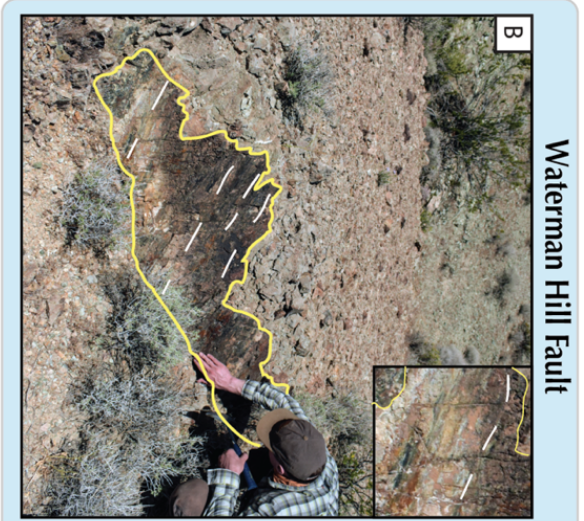
182 The collected hand samples were cleaned of any loose debris and dirt prior to any surface
183 measurement. After surface measurements are performed, we prepared 20 thin sections
184 perpendicular to the plane of the slip surface following (Tikoff et al., 2019) orientation convention,
185 where *XZ* and *YZ* correspond to thin sections oriented parallel and perpendicular to the slip
186 lineations, respectively.

187

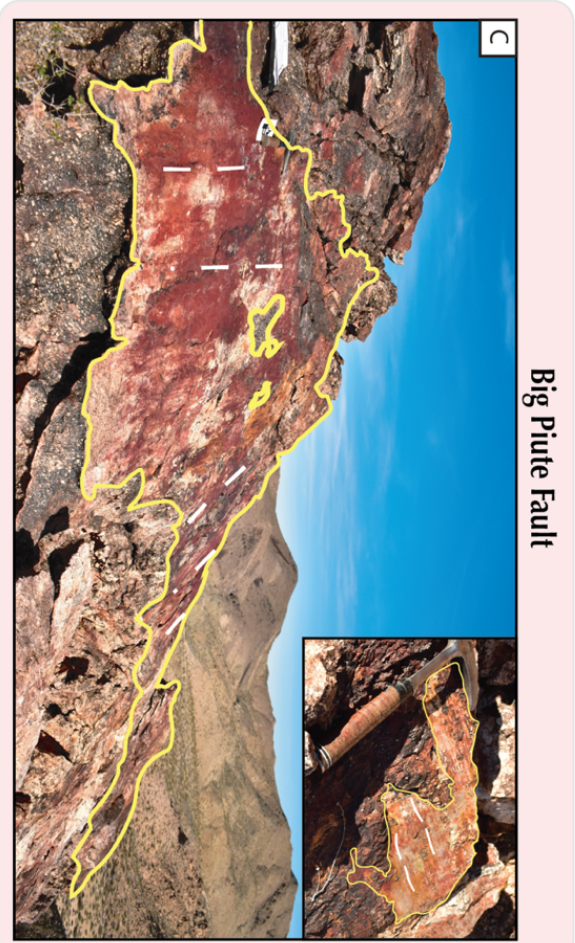
188



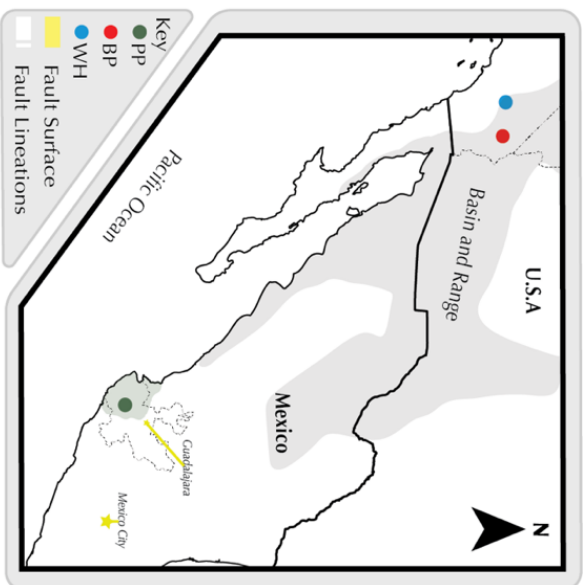
Plan de los Plátanos Fault



Waterman Hill Fault



Big Pute Fault



Plan de los Plátanos (PP) Fault

Location of Main Fault: NW of Autlán de Navarro, Jalisco, Mexico
Tectonic setting: Strike-Slip Faulting
Dominant Lithology: Porphyritic Andesite
Displacement of Main Fault: ~430m
Orientation of Sampled Fault Plane: 80°/114°
Sampling details: Slip surface of a minor splay

Big Pute (BP) Fault

Location of Main Fault: Big Pute Range, Mojave Preserve, SE California
Tectonic setting: Low angle normal faulting
Dominant Lithology: Quartzite
Displacement of Main Fault: unknown
Orientation of Sampled Fault Plane: 30°/72°
Sampling details: Small subsidiary Fault within damage zone

Waterman Hill (WH) Detachment Fault

Location: N of Barstow, SE California
Tectonic setting: Low angle normal faulting
Dominant Lithology: Mylonitized metasedimentary
Displacement of Main Fault: ~40km
Orientation of Sampled Fault Plane: 58°/334°
Sampling details: Minor fault within mylonitic footwall

190 **Figure 1.** Studied fault surfaces. Yellow line highlights slip surfaces and white dotted lines
191 indicate slip lineations. A) Slickensides at the right lateral strike-slip, Falla de Plan de los Plátanos,
192 ID card for scale (8.56 cm long). B) Minor slip surface cutting through the mylonitic footwall of
193 the WH. C) Subsidiary fault within the BP fault damage zone. Insets are close-ups of sampled
194 regions.
195

196 **2.3 Roughness analysis**

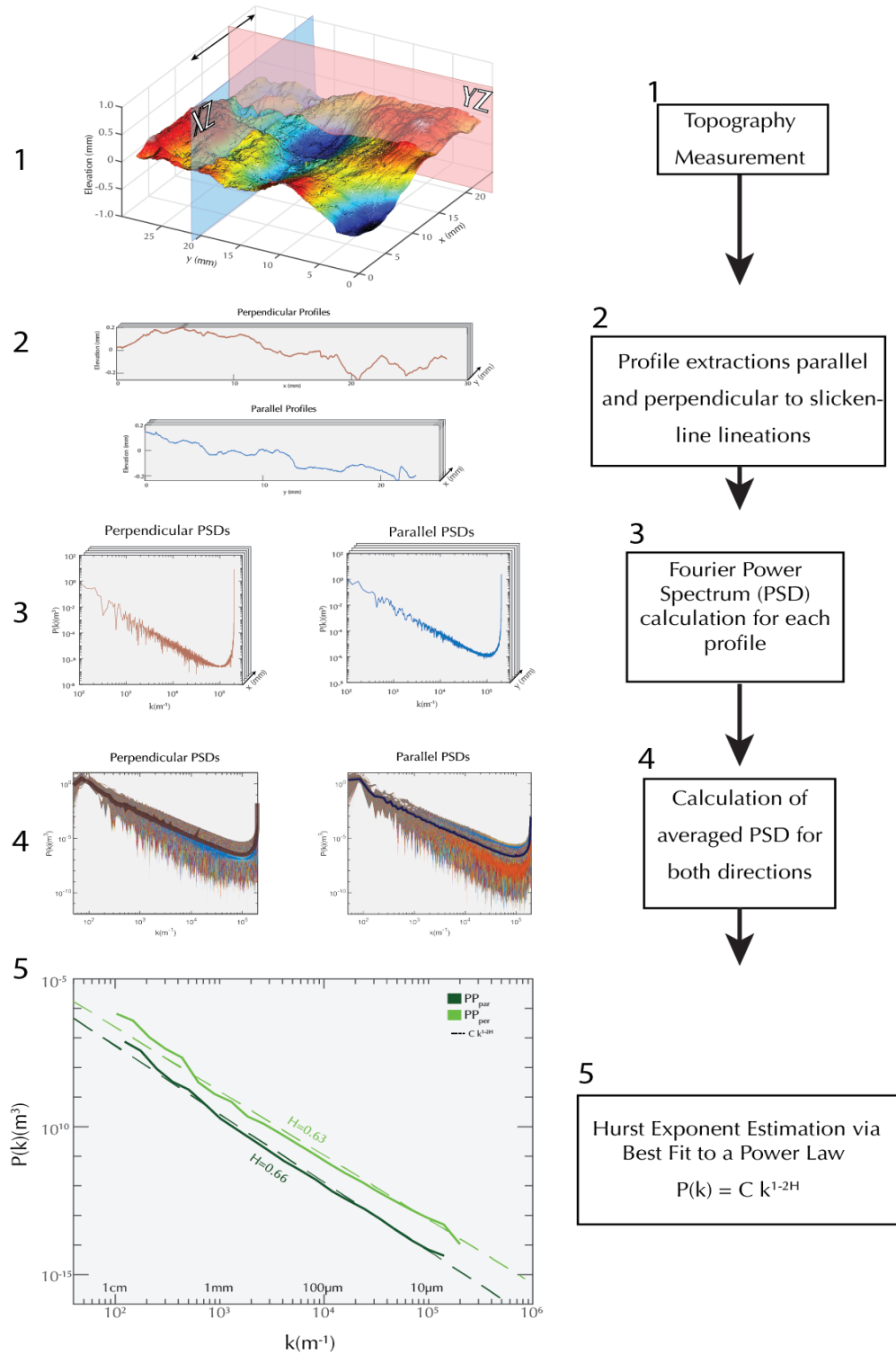
197 We characterized and quantified the slickenside roughness of the different fault surfaces
198 over six orders of magnitude in length scale ranging from 100's of nm to 3 cm. Each surface
199 (between 100 mm² to 1000 mm²) was measured by a Taylor Hobson TALYSCAN 150
200 profilometer using a no-contact laser gauge with a 252 nm vertical resolution. A constant 2 mm s⁻¹
201 ¹ traversing speed and a 5 μm spacing were used for each measurement unless otherwise indicated.
202 At the micron scale, the slip surfaces' topography was measured by manually tracing the surface
203 profile of selected thin sections imaged through Scanning Electron Microscopy (SEM).

204

205 **2.3.1 Hurst Exponent Calculation**

206 The TALYSCAN 150 measurements were processed in MATLAB to remove any planar
207 inclination trend associated with the initial sample placement on the profilometer. 1) The
208 measurements- in the form of an elevation matrix- are then rotated such that the horizontal axis (x -
209 axis) of the 3D and digital elevation models (DEM) are parallel to the slip lineations. Once the
210 trend has been removed from the elevation matrices, we proceeded to calculate the Hurst exponent
211 using power spectrum density analyses (PSD) (c.f., Bistacchi et al., 2011; Candela et al., 2009,
212 2012; Jacobs et al., 2017; Siman-Tov et al., 2013). Profiles parallel and perpendicular to the slip
213 lineations are extracted from each surface. A one-dimensional Hann window function is then
214 applied to each line scan to correct for measurement artifacts, particularly near the edges, as
215 suggested by Jacobs et al., (2017). 3) The Fourier power spectrum $P(k)$ is calculated for each
216 profile as a function of wavenumber (k) and normalized by dividing the power spectrum by the
217 length of the corresponding profile. 4) The power spectra for both the parallel and perpendicular

218 directions to slip are averaged at each wavenumber to reduce noise associated with each individual
219 profile. 5) The Hurst exponent is then calculated from the best fit to a power-law of the form
220 $P(k)=Ck^{1-2H}$, where H is the Hurst exponent, and C is the pre-factor. The workflow is illustrated in
221 Fig. 2.
222



224

225 **Figure 2.** Calculation of Hurst Exponent. See text for details.

226

227 **2.3.2 Multiscale Surface Texture Analysis**

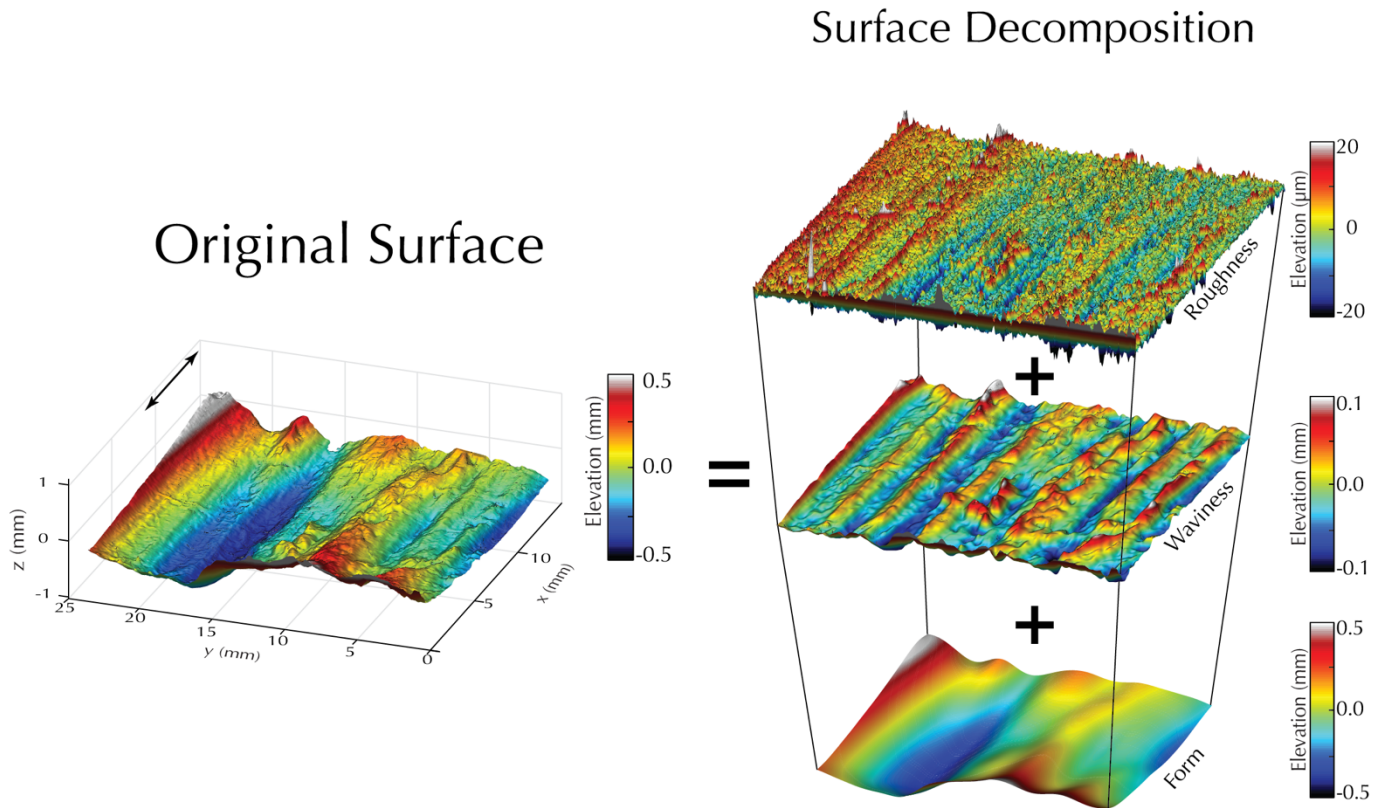
228

229 Given that the roughness measurements are inherently a superposition of surface texture
230 information from different length scales, we performed a multiscale surface texture analysis
231 (MSA) in addition to the Hurst exponent calculation. A MSA consists of decomposing the surface
232 topography at various cutoff wavelengths to separate the surface texture into 1) *form*, 2) *waviness*
233 (macro-roughness), and 3) *roughness* (micro-roughness) as shown in Fig. 3 (C. A. Brown et al.,
234 2018). We used a Gaussian 2D filter to separate the data into three different bandwidths with cutoff
235 wavelengths centered at 5 mm and 500 μm . Care is taken that the energy of the signal is preserved,
236 i.e., that the original signal can be fully reconstructed when all components are added together.
237 Furthermore, for each component, we calculate the kurtosis (S_{kur}) and skewness (S_{sk}) of the height
238 distribution.

239

240

241



242 **Figure 3.** Schematic of a Multiscale Surface Texture Analysis shows how a surface measurement

243 is decomposed into characteristic wavelengths.

244

245 **2.4 Microstructural Analyses**

246 We aim to identify the microphysical processes occurring within the slickenside volume
247 and adjacent fault rocks. We study a) the grain size distributions and b) the morphologies and
248 crosscutting relationships preserved in, and adjacent to the slickensides to reveal their relationship
249 to fault surface development.

250

251 **2.3.1 Imaging conditions**

252 Thin sections oriented parallel (*XZ*) and perpendicular (*YZ*) to the slip direction were
253 analyzed using a ZEISS AX10 Petrographic microscope and ZEISS Merlin HR-SEM equipped
254 with a Backscattered electron (BSE) detector.

255 The SEM was operated with a beam current of 5 nA and a 15 kV accelerating voltage unless
256 otherwise indicated. To capture the range of structures and grain sizes, images were acquired at
257 various magnifications resulting in a 0.77 nm/px to 2.06 $\mu\text{m}/\text{px}$ resolution.

258

259 **2.2.2 Grain Size analysis**

260 Grain size measurements were obtained by manually tracing petrographic microscopy and
261 BSE images obtained at progressively higher magnifications as illustrated in Fig. 4. At each
262 magnification we trace the maximum number of discernible grains/clasts, typically 300-3000
263 segmented grains per image range are used. Segmented images were then imported to *ImageJ* to
264 calculate the area (*A*) of each grain in pixels. Grains with areas smaller than 20 pixels, i.e., the
265 smallest grain size that could still be clearly recognized as such, were excluded. The size of each
266 grain is then approximated by calculating the diameter of a circle with the same area. The
267 equivalent diameters (d_{eq}) were calculated as

268
$$d_{eq} = 2\sqrt{\frac{A}{\pi}}, \quad (1)$$

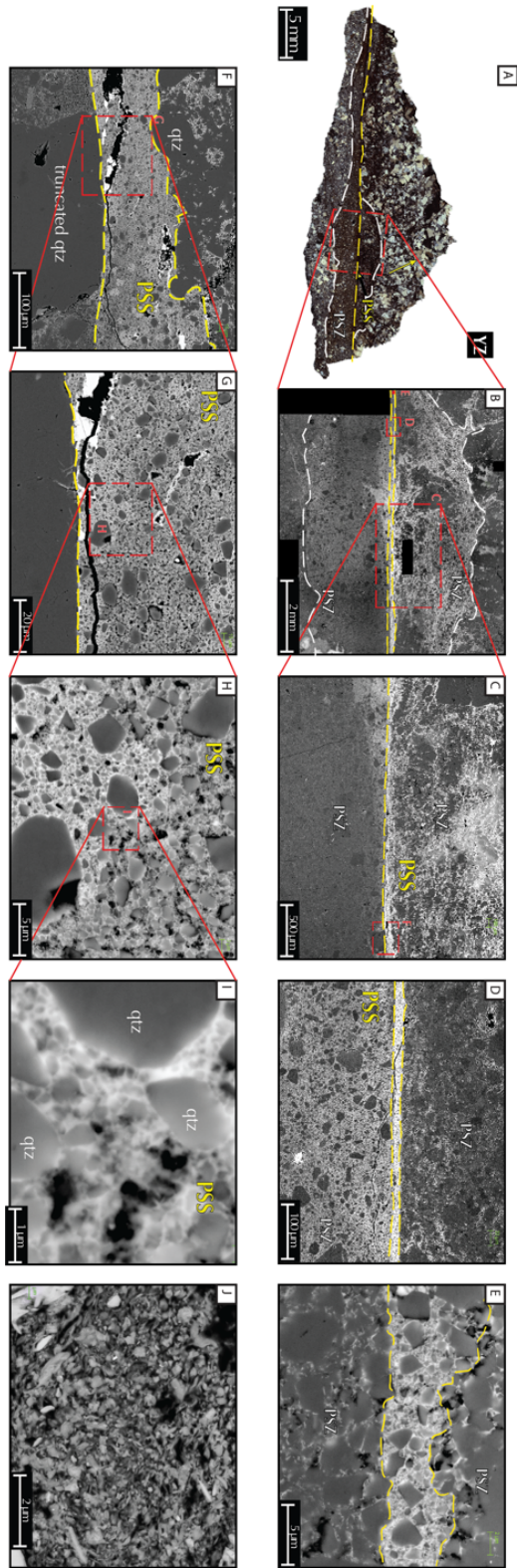
269 and collected in a histogram with twenty bins for each magnification.

270 The bins from each magnification are plotted in a logarithmic scale to determine the slope (S_n)
271 and intercept (I_n) of the best power-law fit. The frequency of each bin is then multiplied by a factor
272 (L_n) that reflects the relative magnification at each image to correct for undercounting of the total
273 number of grains from analyzing progressively smaller areas. The factor, L_n , is determined by:

274
$$L_n = 10^{I_{max} - I_n}, \quad (2)$$

275 where I_{max} corresponds to the intercept of the lowest magnification. The results from all
276 magnifications are then combined into a single plot.

277 D-values of 0-2 are commonly measured in two-dimensional analyses (e.g., analysis of SEM
278 images) and correspond D-values between 1-3 from three dimensional analyses such as sieving
279 and Coulter counting (Glazner & Mills, 2012). To draw comparison with D-values reported in
280 other studies that utilized three-dimensional methods the following conversion, $D_{2D} = D_{3D} - 1$, from
281 Heilbronner & Barrett (2014) is used.



282 **Figure 4.** Set of images at progressively higher magnifications used in the GSD determination of
 283 quartzite hosted slickenside. See text for details.
 284

285 **3. Results**

286 **3.1 Roughness Analysis**

287 Roughness plays a significant role in the contact behavior of surfaces and is usually
288 described as the deviations normal to a surface. We analyzed the roughness of our slickenside
289 samples using the Fourier power spectrum density (PSD) approach to calculate their respective
290 Hurst exponents followed by a multiscale analysis of the surfaces' height distributions.

291 In Figure 5 we show the wide variety of surface textures that can be qualitatively grouped into two
292 general domains, “*smooth*” and “*rough*”, based on the amplitudes and frequency of the dominant
293 asperities.

294

295 **3.1.1 Power Spectral Density Results**

296 The averaged power spectral density (PSD) curves for all roughness measurements are
297 shown in Fig. 6. PSDs are obtained from profiles scanned parallel (*par*) and perpendicular (*per*) to
298 the slip lineations, i.e., the *x*- and *y*-directions, as illustrated in Fig. 2.

299 Spectra for most measurements show only limited variability in the slope of profiles measured
300 parallel to lineations with a mean Hurst exponent of 0.53 ± 0.07 and a range of 0.41-0.63. In
301 contrast, the perpendicular profiles showed a wider variability with values of H_{per} ranging from
302 0.45-0.72 and a mean of 0.60 ± 0.10 . The pre-factor is directly proportional to root mean squared
303 roughness (*RMS*) by

304
$$RMS = \sqrt{\left[\frac{Ck^{-2H}}{-2H} \right]_{k_{min}}^{k_{max}}} \quad (3)$$

305 And thus, a higher C indicates overall higher roughness amplitude, whereas a lower H indicates a
 306 larger contribution of smaller wavelengths/higher spatial frequency, i.e., surfaces relatively
 307 rougher at smaller length scales than a self-similar surface ($H = 1$) with the same C would be.
 308 While the samples studied in this paper show a relationship between the pre-factors and H , the
 309 inclusion of measurements from Bistacchi et al., (2011) and Candela et al., (2013) indicates no
 310 clear trend (Fig 6B). Furthermore, measurements of the various hand samples obtained from the
 311 same fault surface show a wide range in both H and C values, Table 1.

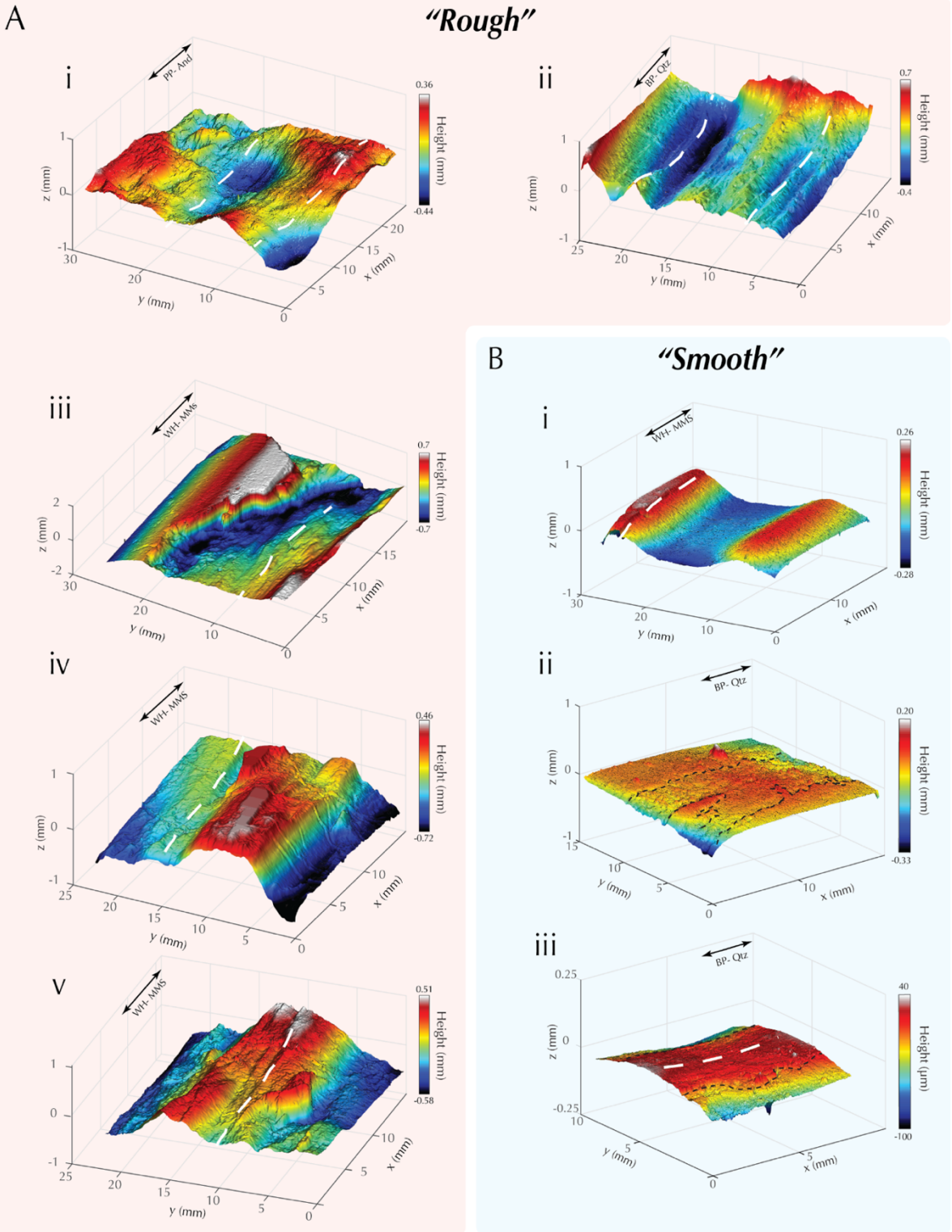
312
 313

314 **Table 1.** Hurst (H) and Pre-exponent (C)

Fault	H_{par}	H_{per}	C_{par}	C_{per}
Plan de los Plátanos				
	0.61	0.58	2.5×10^{-3}	2.2×10^{-3}
Big Piute				
Min	0.41	0.45	3.4×10^{-5}	2.2×10^{-3}
Max	0.52	0.72	2.2×10^{-3}	1.8×10^{-2}
Waterman Hill				
Min	0.51	0.48	4.9×10^{-4}	2.2×10^{-3}
Max	0.65	0.71	3.5×10^{-2}	6.2×10^{-2}

315

316

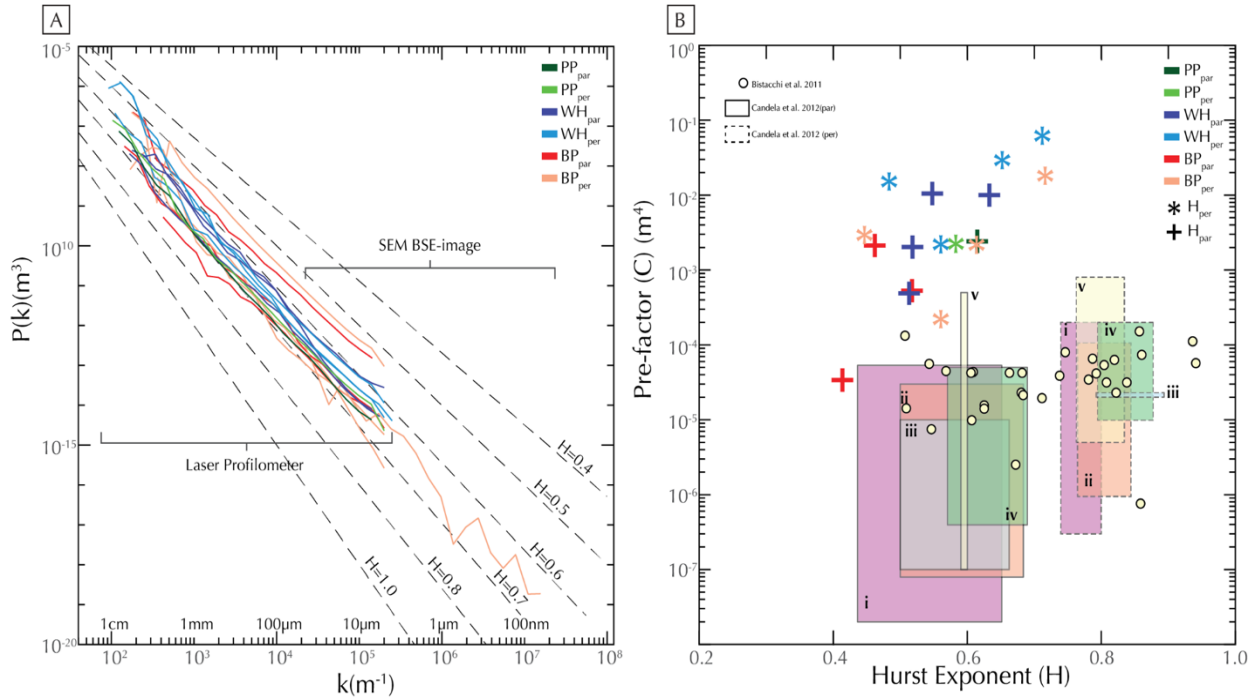


317

318

319 **Figure 5.** Topography of the different surfaces collected via laser profilometry qualitatively
320 grouped in A) rough and B) smooth surfaces. White dotted lines highlight grooves and lineations.
321 Black dotted lines highlight transitions in roughnesses. PP-, WH-, and BP- indicate the fault
322 system, whereas And (andesite), MMS (mylonitic meta-sedimentary), and Qtz (quartzite) indicate
323 the respective lithologies.

324



325

326 **Figure 6.** Results from PSD analysis. A) Shows the Fourier power spectra for all studied samples.

327 Note similar slopes fit most samples; rougher samples plot higher in the graph. B) Pre-factor and

328 Hurst exponents obtained from (A), Gole Larghe Fault Zone (Bistacchi et al., 2011) and i) Bolu,

329 ii) Vuache-Sillingy iii) Dixie Valley iv) Corona Heights and v) Magnola faults (Candela et al.,

330 2012). Note data from (Bistacchi et al., 2011) does not specify direction of slip (circles), whereas

331 data from (Candela et al., 2012) is plotted as a range from minimum to maximum values for H and

332 C for both parallel (filled square) and perpendicular (squares with dash lines) directions to slip.

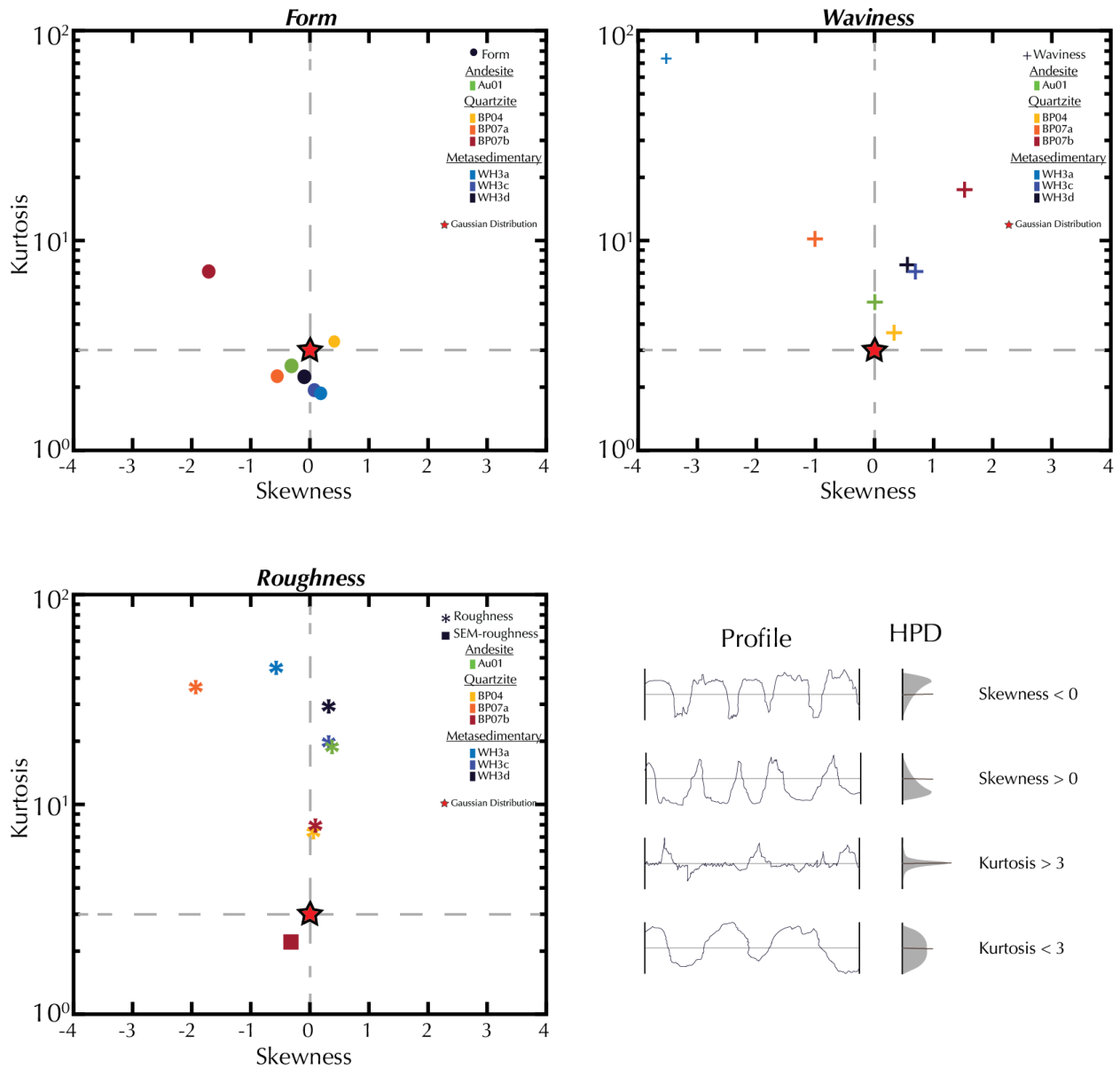
333

334 3.1.2 Height Distributions

335

336 Skewness (S_{sk}) and kurtosis (S_{kur}) are statistical measures that describe the symmetry and
337 peakedness of the height distributions. A distribution is known as a Gaussian when $S_{sk}=0$ and
338 $S_{kur}=3$. A high kurtosis ($S_{kur}>3$) corresponds to a distribution with a greater peakedness than a
339 Gaussian, which indicates more height measurements are centered near the mean height, whereas
340 the converse is true for a low kurtosis ($S_{kur} <3$). Furthermore, a positive and negative skewness
341 indicates most measurements lie either below or above the mean surface, respectively, as
342 illustrated in Fig. 7A. The samples show a wide range of S_{sk} and S_{kur} values, with no systematic
343 variation with respect to lithology or fault system. However, samples wherein lineations are more
344 apparent and visually rougher tend to have more positive skewness whereas, kurtosis is generally
345 higher for smoother samples. The departure from a Gaussian height distribution also appears to be
346 affected by the scale of observation with smaller wavelength having overall higher kurtosis values
347 as documented in Fig. 7A-C. Note also surface decomposition in Fig. 3, which illustrates the
348 distinct roughness at different scales.

349



351

352 **Figure 7.** Skewness and kurtosis for samples A) *Form*, B) *Waviness*, and C) *Roughness*. D)
 353 Schematic surface profiles with positive and negative skewness and kurtosis values higher and
 354 lower than three, after Gadelmawla et al., (2002).

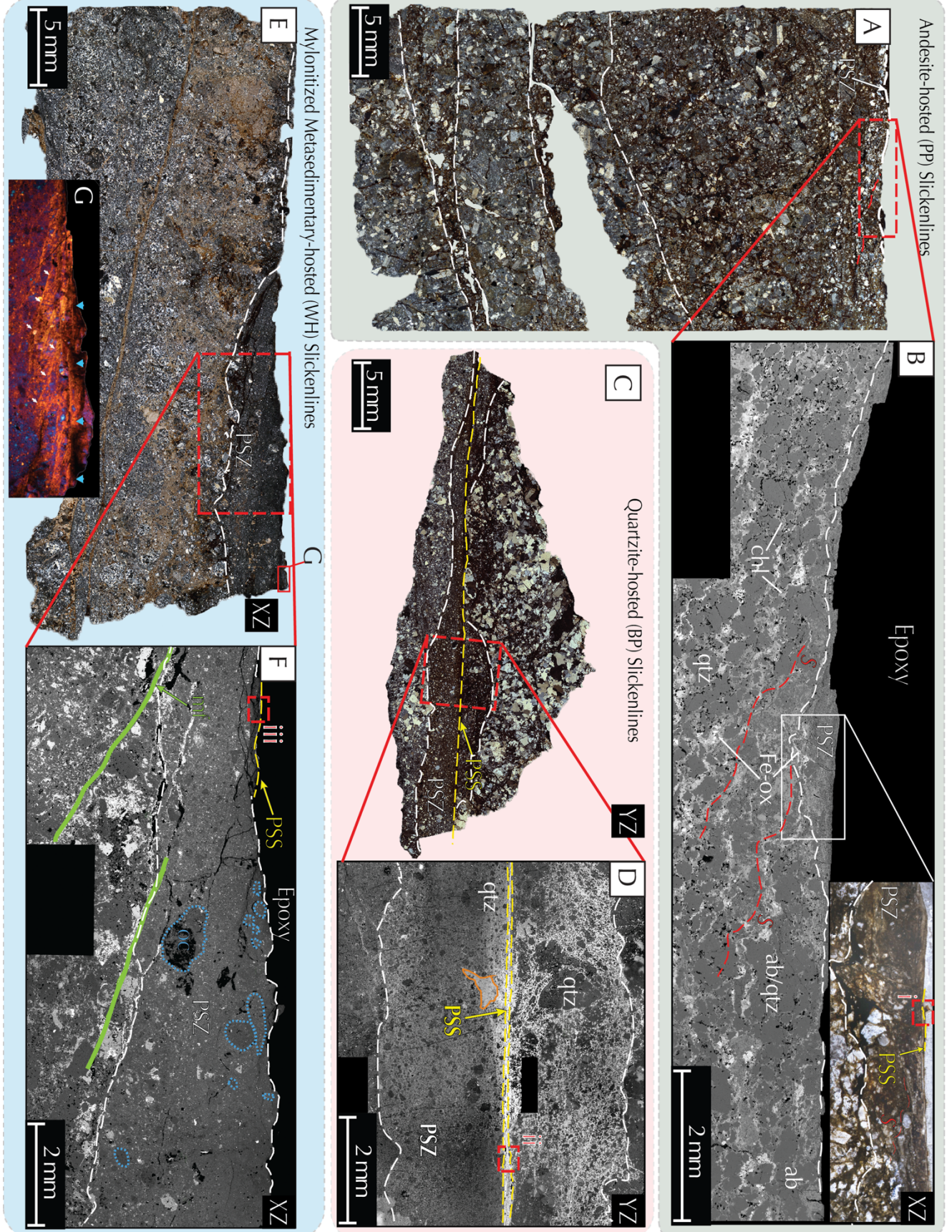
355

356 **3.2 Structural and Microstructural Observations**

357 With the aim of interpreting the processes involved in fault slip and slickenside
358 development, we selected one sample from each locality that best preserves the slickenside
359 features to conduct SEM-BSE imaging and describe the microstructures in greater detail. We
360 focused on the morphologies at the surface and throughout the rock volume adjacent to the slip
361 surface. For each sample, we specifically examine a) the size and spacing of the lineations, b)
362 orientation of structures on the slip surface, c) the structures within the host rock immediately
363 adjacent to the slip surface, and d) the grain size distribution.

364

365



367

368 **Figure 8.** Selected samples for microstructural analysis. White and yellow dashed lines highlight
369 Principal Slip Zones (PSZ) and Principal Slip Surfaces (PSS), respectively. A) Andesite hosted
370 slickenside thin sections under cross-polarized light (XPL). Note relatively undeformed primary
371 igneous fabric at the bottom of the image and multiple slip zones. B) SEM-BSE close-up of A.
372 characterized as a zone of highly comminuted grains of irregular thickness. Dark grey colors
373 correspond to quartz (qtz) and albite (ab), bright grey chlorite (chl), white Fe-ox, whereas black
374 spots within the rock volume correspond to porosity. Note S-C cataclasite with top to the left sense
375 of shear. Inset: plane polarized light (PPL) close-up of PSZ fluidized ultra cataclasite. Note tails
376 around larger clasts. C) Quartzite hosted slickensides under XPL, preserving opposing segments
377 of the fault surface. D) SEM-BSE close-up of C. Note the principal slip zone (PSZ) is characterized
378 by highly comminuted grains in the μm -size range, whereas the principal slip surface (PSS-yellow)
379 is localized to few tens of microns and decorated by an abundance of Fe-oxide minerals (bright
380 colors). Note asymmetry in Fe-oxide distribution and comminution between both sides of the fault.
381 Charging artifact denoted by orange lines. E) Slickenside hosted in mylonitic metasediments under
382 XPL. F) Close-up of E shows the presence of a Principal Slip Zone (PSZ) of variable thickness
383 characterized by sharp grain size reduction towards the slip surface and towards a thin Principal
384 Slip Surface (PSS). Note the presence of older cataclastic clasts (OC) within the PSZ. Micro-faults
385 (mf-green) are also observed offsetting the PSZ. G) Close-up of E under XPL with gypsum lambda
386 plate inserted highlights region adjacent to surface where localized shear bands (two main
387 orientations outlined by white and teal arrows) exhibit strong and spatially coherent optical
388 anisotropy.

389

391 **Figure 9.** Photomicrographs of foliated cataclasites with S-C-C' fabrics under plane polarized
392 light (PPL). S-, C- and C'- planes outlined by dotted red, yellow, and black lines, respectively.
393 Vertical shaded strips are artifacts from stitching of images. PSZ outlined by thin white dashed
394 line characterized by a sharp decrease in grain size. Note C-planes are parallel to PSS and
395 undulation in PSZ contact follow the edges of S-, C-, and C'-planes. Slickenside hosted in A-B)
396 Quartzite and C-D) mylonitic metasedimentary rocks

397 3.2.1 Plan de los Plátanos Fault

398 The main slip surface is covered by a thin film that is glossy and smooth, with specularly
399 reflective patches. The lineations have an average width of $527 \pm 83 \mu\text{m}$ and spacing of $0.85 \pm$
400 0.18 mm that remain relatively constant throughout the length of the sample (Fig. 5A). Secondary
401 fractures perpendicular and diagonal to the lineations crosscut the surface.

402 Below the exposed surface, we identified S-C-like fabrics and a quartz-rich vein with
403 predominantly ductile fabrics that soles into the slip surface. The quartz grains are elongated,
404 exhibit undulose extinction and host multiple inclusions. All fabrics are then cut by a principal slip
405 zone (PSZ) comprising a fluidized ultracataclasite of variable thickness ($100\text{-}500 \mu\text{m}$) that is
406 characterized by a sharp decrease in grain size from the host rock towards the slip surface (Fig.
407 8A-B). In addition to the main exposed surface, other minor slip surfaces were identified splaying
408 within the sample.

409 The PSZ features a quartz-rich zone ($\sim 10 \mu\text{m}$ thick) of increased cohesion (ICZ) next to the
410 surface, wherein grains exhibit serrated, interlocked grain boundaries, triple junctions, and
411 sintering microstructures, followed by sharp break towards a $\sim 5 \mu\text{m}$ thin principal slip surface
412 (PSS) (Fig. 10A and Fig. 11A).

413 The PSS is characterized by a predominance of mostly rounded submicron-size grains/particles
414 embedded within “*wispy*” phyllosilicate-like matrix enriched in Al and Fe compared to the PSZ
415 (Fig. 10A-Fig 11A). In regions where the PSS is thicker, the PSS exhibits a denser morphology
416 with little to no porosity, albeit fractured, with similarly rounded nm-size grains/particles as well
417 as elongated grains preferentially aligned subparallel to the surface (Fig. 10B).

418

419 3.2.3 Big Piute Slickensides

420 The slip surfaces are flat and smooth, i.e., no grooves are perceived with the naked eye,
421 particularly in the direction parallel to the lineations. Iron-oxides (Fe-ox) decorate the slip surfaces,
422 including botryoidal hematite. The lineations are marked by alternating smeared Fe-ox bands with
423 a spacing of 8.2 ± 0.5 mm and 1-3 mm wide grooves (Fig. 5 Bii-iii).

424 Across the XZ orientation, the sample exhibits a foliated cataclasite microstructure with an S-C-
425 C' fabric that transitions into the PSZ and PSS (Fig 9A-B). The foliations are defined by sigmoidal
426 dark brown layers that bound asymmetric quartzite clasts and clast aggregates with their *tails*
427 preferentially oriented $\sim 45^\circ$ to the fault surface (S-foliation), C'-shear bands developed oblique to
428 the S- and C- orientations, and localized micro-shears sub-parallel to the slickenside surface (C-
429 surface) (F. M. Chester et al., 1985; A. Lin, 2001; Passchier & Trouw, 2005). The waviness of the
430 contact between the host rock and the PSZ follows the orientation of the S-, C-, and C'- planes.

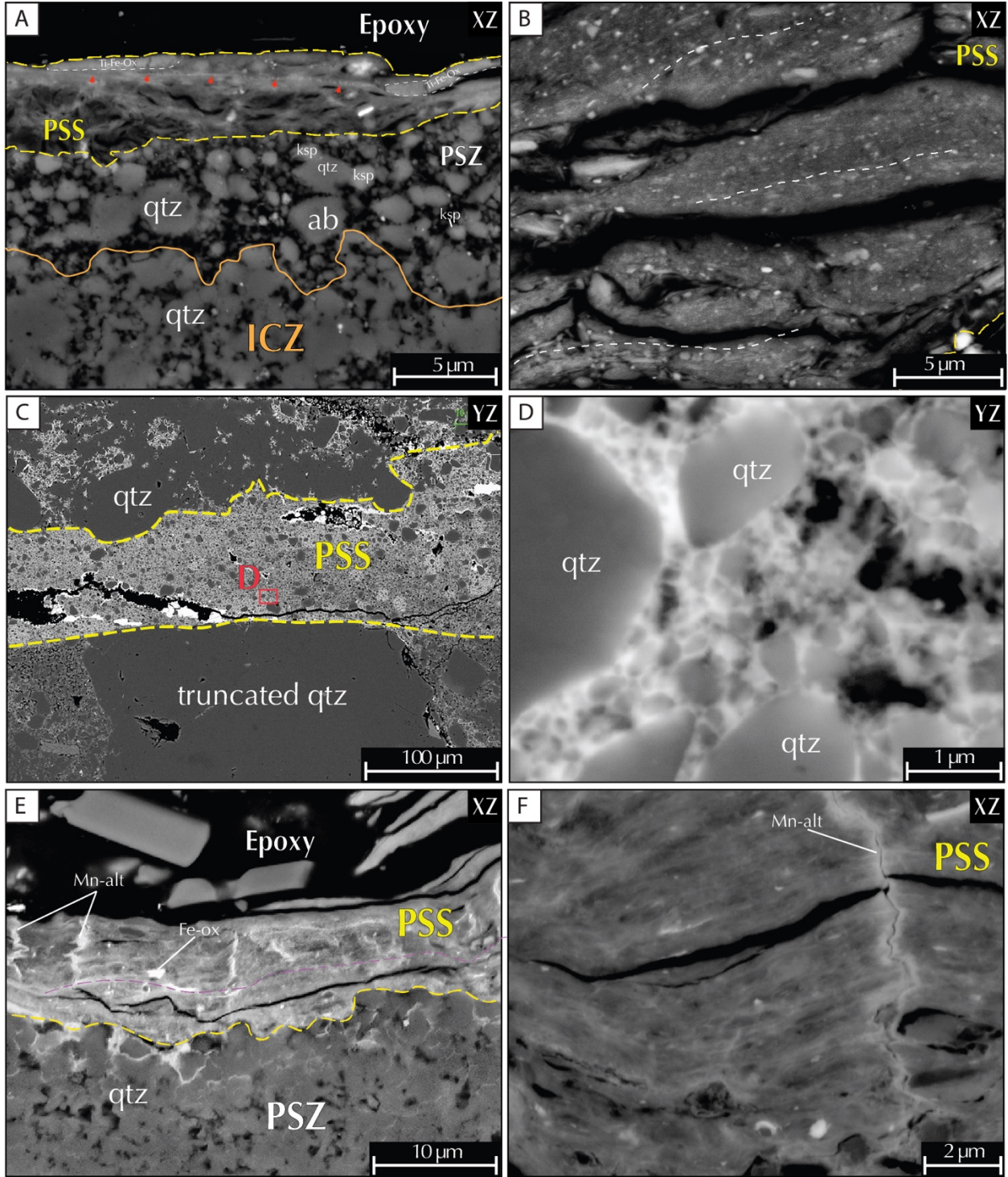
431 The clast size of the cataclasite and spacing between S-C-planes gradually fines and rotate until it
432 transitions into an ultracataclasite that makes up the PSZ and a 18 ± 11 μm thin PSS. (Figs. 8C-D,
433 9A-B, and 10C-D). The PSS is characterized by truncation and plucking of grains from the PSZ
434 and matrix comprising rounded nanometric grains with little to no fractures cemented by a matrix
435 of Fe-ox. Void spaces along fractures within the PSS are then filled by an alternating growth of
436 Fe-ox and quartz, (Fig 10C).

437

438 **3.2.3 Waterman Hill Slickensides**

439 The surface forms a resistant ledge, is smooth and specularly reflective. The lineations are
440 marked by cm-scale undulations within mirror-polished regions and by 520 ± 160 μm wide
441 grooves in portions of the surface that are not specularly reflective.

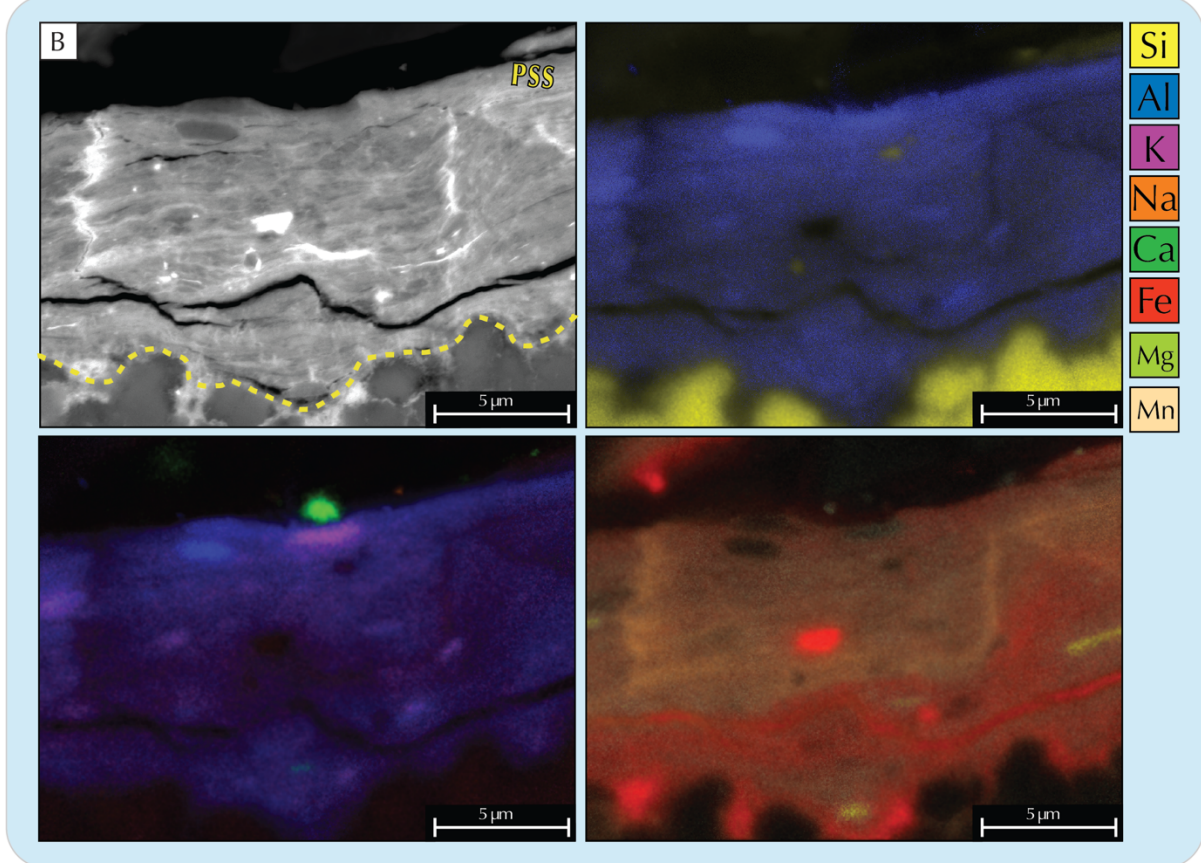
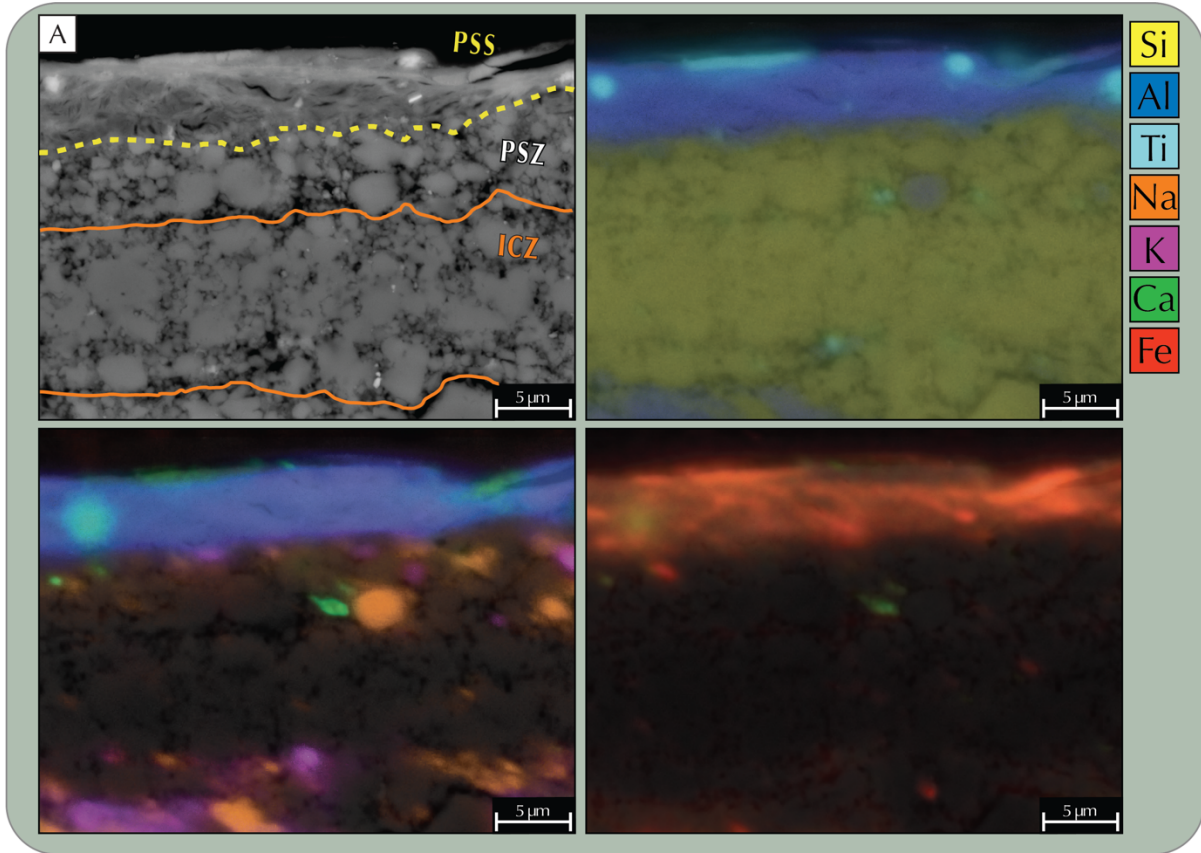
442 We observe that the WH slickenside samples also exhibit a region of extremely comminuted
443 grains, PSZ, adjacent to the slip surface, and S-C-like fabrics throughout its host rock. Unlike the
444 other samples, the PSZ here varies significantly in thickness, from $\sim 100 \mu\text{m}$ to 5 mm, along the
445 direction of slip (XZ). Regions where the PSZ is thicker coincide with numerous micro-faults that
446 displace the PSZ but do not crosscut the mirror-polished surface. The PSZ contains clasts of earlier,
447 more consolidated cataclasites (OC). Immediately adjacent to the slip surface, two main features
448 are prominent: a) the presence of Reidel-like and boundary (subparallel to the slip surface) shear
449 bands that exhibit extreme grain size reduction and uniform optical anisotropy, Fig. 8E, and b) a
450 dense thin film (PSS) that coats the PSZ that features elongated grains preferentially oriented
451 subparallel to the surface embedded within a potentially partially amorphous matrix, Fig. 10F,
452 similar to Fig. 10B. Nanosized grains are also observed to be common within the matrix of the
453 PSZ.
454



455

456

457 **Figure 10.** SEM-BSE images of the Principal Slip Zones. **Andesite hosted slickensides:** A-B)
458 SEM-BSE operated with 20 kV accelerating voltage and 8.0 nA beam current. A) Close-up of PSZ
459 in Fig 8B.i, showing the presence of a thin PSS and a quartz-rich Increased Cohesion Zone (ICZ)
460 and PSS. Note the PSS is a thin layer (a few microns thick) comprising a randomly oriented Al-
461 and Fe-rich “wispy” phyllosilicate-like matrix and submicron sized particles. Note the roundness
462 of most clasts and Fe-rich veinlet in PSS, red arrows. The ICZ is characterized by a decrease in
463 porosity, grains with irregular and serrated grain boundaries, and sintering microstructures. B)
464 Close-up of dense region of PSS. Note the presence of rounded nano-sized particles and elongated
465 preferentially oriented grains, highlighted by white dashed lines. **Quartzite hosted slickensides:**
466 C) Close-up of the PSS from Fig 8D.ii. Image shows a sharp decrease in grain size from the PSZ
467 (outside of the yellow boundary) towards the PSS, which is characterized by a Fe-oxide-rich layer
468 of micron-sized grains supported in a fine grain matrix. Note truncation of quartz clast by the PSS.
469 D) Close-up of PSS matrix shows matrix comprises predominantly submicron-sized qtz grains and
470 Fe-ox cement (bright colors). Note roundness and lack of fractures on matrix grains and euhedral
471 growth of Fe-oxide blades into void spaces. **MMS hosted slickensides:** E) Close-up into the PSS
472 Fig 8F.iii, shows it comprises a dense layered possibly amorphous matrix with rounded grains and
473 preferentially oriented elongated grains. Note bright vertical features enriched in Mn. Layering is
474 highlighted by a magenta dotted line. F) Close-up of PSS. Note dense matrix with little to no
475 porosity and sub-micron rounded grains.



477 **Figure 11.** Compositional EDS maps of Principal Slip Surfaces. A) Andesite hosted slickensides:
478 from Fig. 10A Note Si-rich (quartz) Increased Cohesion Zone (ICZ) and Al, Fe and Ti enriched
479 PSS. B) MMS hosted slickensides: Close-up of PSS in Fig 10E showing PSS is enriched in Al, Fe.
480 Bright fractures enriched in Mn. Note thin Al-, K-, and Mg-rich rods preferentially aligned
481 subparallel to the slip surface.

482 3.3 Grain Size Distribution

483 To characterize the comminution processes occurring during slip, we analyzed the grain
484 size distribution of the fault rocks adjacent to the slip surface. Here we present the results of the
485 grain size analyses performed on two sequences of petrographic microscopy and SEM images
486 taken at increasing magnifications from selected samples from the BP and PP faults. The results
487 are plotted on log-log plots of frequency vs. equivalent diameter to determine the fractal grain size
488 distribution (GSD), Fig. 12.

489 We did not perform grain size analysis on samples from the WH Fault. It was not possible to
490 accurately identify individual grain boundaries as the particles appear embedded within a cement
491 of similar composition. Furthermore, when the boundaries between particles could be accurately
492 identified, they exhibit interlocked grain boundaries, suggesting static crystal growth and healing
493 (Keulen et al., 2008), and thus obscuring the grain sizes related to the comminution process.

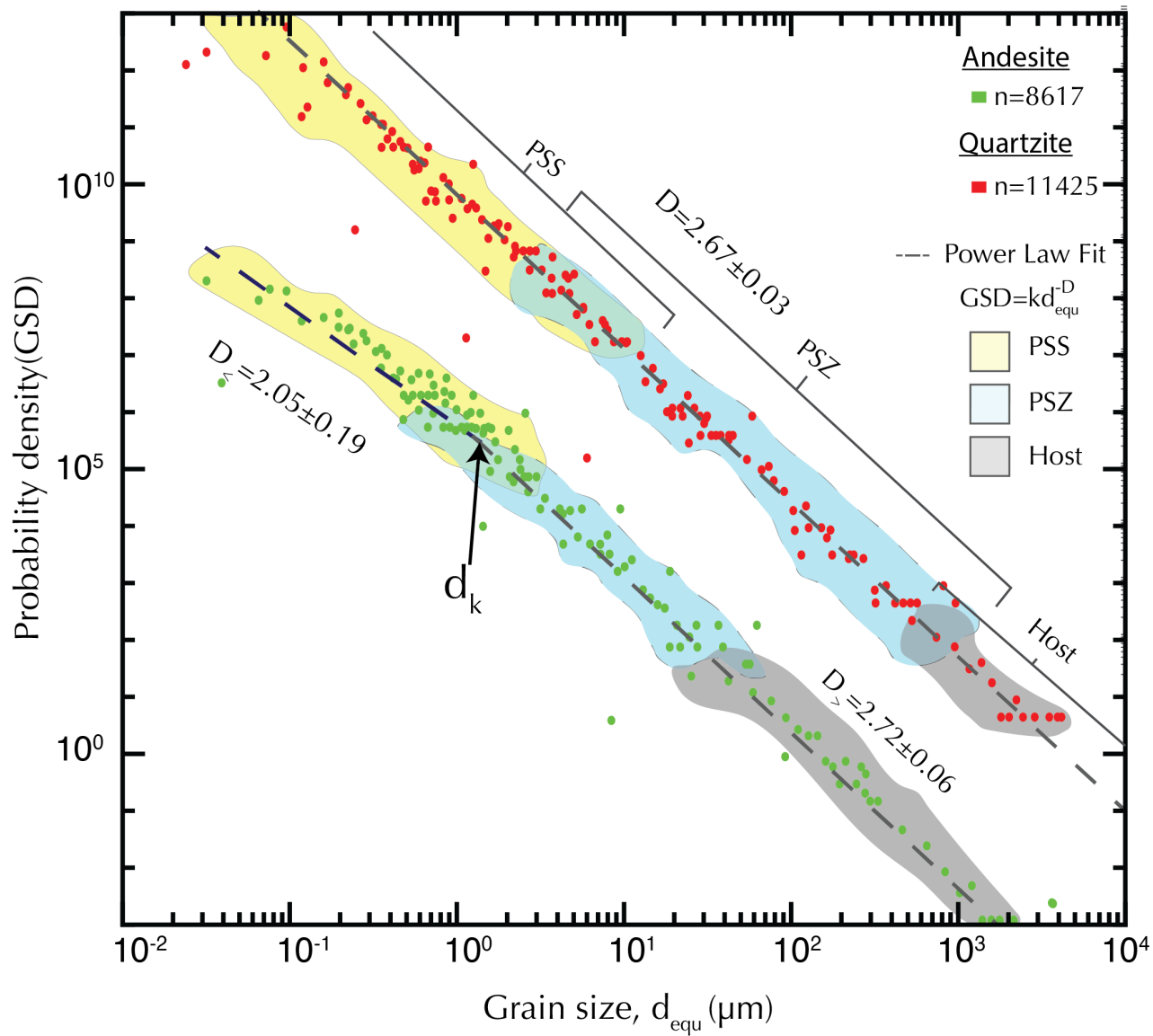
494 The grain size distribution for the quartzite sample shows a power-law functional relationship over
495 six orders of magnitude (10's nm-1's mm) with a constant slope of $D = 2.67 \pm 0.03$ despite the
496 sharp decreases in grain size observed within the transition from the host rock towards the PSZ
497 and PSS respectively, Fig. 8C-D. However, it is observed that at the lower grain size range (less
498 than 100 nm), the distributions start to plateau as the grain size approaches the resolution limit of
499 the SEM (a single pixel at the highest magnification equals 0.77 nm). The smallest grain sizes are
500 found within the unconsolidated gouge with an equivalent $d_{min} = 18 \text{ nm}$, whereas the smallest
501 observable grains within the matrix of the PSS corresponded to 30 nm.

502 In contrast to the monomineralic quartzite, the andesite hosted slickensides exhibit two distinct
503 parts that can be discriminated by a break in the GSD slope. Two D -values are obtained: a lower,
504 $D_{<} = 2.05 \pm 0.19$ for small grain sizes ($d < d_k$), and $D_{>} = 2.72 \pm 0.06$, for large grain sizes ($d > d_k$),

505 where $d_k \approx 2 \mu m$ and is the grain size at the intersection of the two curve fits. This intersection (dk)
506 occurs where grains measured only in the PSS and PSZ overlap. Within the small grain size range,
507 the smallest grains are found embedded within the PSS matrix with a $d_{min}=30 nm$.

508

509



510

511

512 **Figure 12.** Grain Size Distributions of quartzite (red) and andesite (green) host rocks. Data has
513 been displaced vertically for clarity. The GSD of quartzite samples can be described by a single D
514 $= 2.67 \pm 0.03$, whereas GSD has two distinct slopes for $D_{<} = 2.05 \pm 0.19$ and $D_{>} = 2.72 \pm 0.06$ for
515 grain size smaller or larger than $d_k \approx 2 \mu\text{m}$, respectively. The different color envelopes indicate the
516 range of grain sizes found within the PSS, PSZ, and the host rock. Data points outside the color
517 envelopes correspond to artifacts due to the limited resolution in each measured image.

518

519

520 4 Discussion

521

522 This work provides a detailed study of surface roughness of slickensides and the associated
523 microstructures in the surrounding fault rocks from three different fault zones hosted in various
524 rock types that have experienced different deformation histories. The observations from both the
525 surface and respective volume and their implications for our understanding of faulting processes
526 are discussed below.

527

528 Fully characterizing a fault surface is of particular importance for better understanding fault
529 processes. It has been shown that the stress distribution is affected by fault geometry, as the latter
530 controls to a first degree the real contact area (e.g., Ben-Zion & Rice, 1997; Bruhat et al., 2020;
531 Cattania & Segall, 2021; Harbord et al., 2017; Sagy & Lyakhovsky, 2019; Tal et al., 2020). Our
532 current understanding of fault surface geometry is that it is self-affine and that it can be
533 characterized by four parameters (H_{per} , H_{par} , C_{par} , C_{per}) (Brodsky et al., 2016; Candela et al., 2009,
534 2012). In agreement with other reports, our studied fault surfaces further indicate that regardless
535 of lithology or tectonic setting, the roughness of individual fault surfaces exhibits an anisotropic
536 self-affine topography with Hurst exponents (H) and pre-factors (C) within the $0.4-0.8$ range and
537 $10^{-5} - 10^{-2}$, respectively. The surface roughness of our samples, however, consistently exhibited
538 smaller H-values and less anisotropy than most reported natural fault surfaces, i.e., the roughness
539 measured perpendicular- and parallel to the slip lineations exhibited closely valued Hurst
540 exponents with mean $H_{par}=0.53 \pm 0.07$ and $H_{per}=0.60 \pm 0.10$ as opposed to the more commonly
541 reported $H_{par}\approx 0.6$ and $H_{per}\approx 0.8$, (Bistacchi et al., 2011; Candela et al., 2009, 2012; Power & Tullis,
542 1989; Renard et al., 2012; Sagy et al., 2007; Thom et al., 2017; Tisato et al., 2012). The smaller H

543 values likely indicate that our surfaces appear smoother at larger scales and rougher at finer scales
544 than other faults while the reduced anisotropy could be related to inherent heterogeneity within the
545 fault surfaces. Similarly, this discrepancy could also be related to the conditions at which such
546 surfaces were formed and/or altered. While intriguing, our current observations cannot explain this
547 peculiarity.

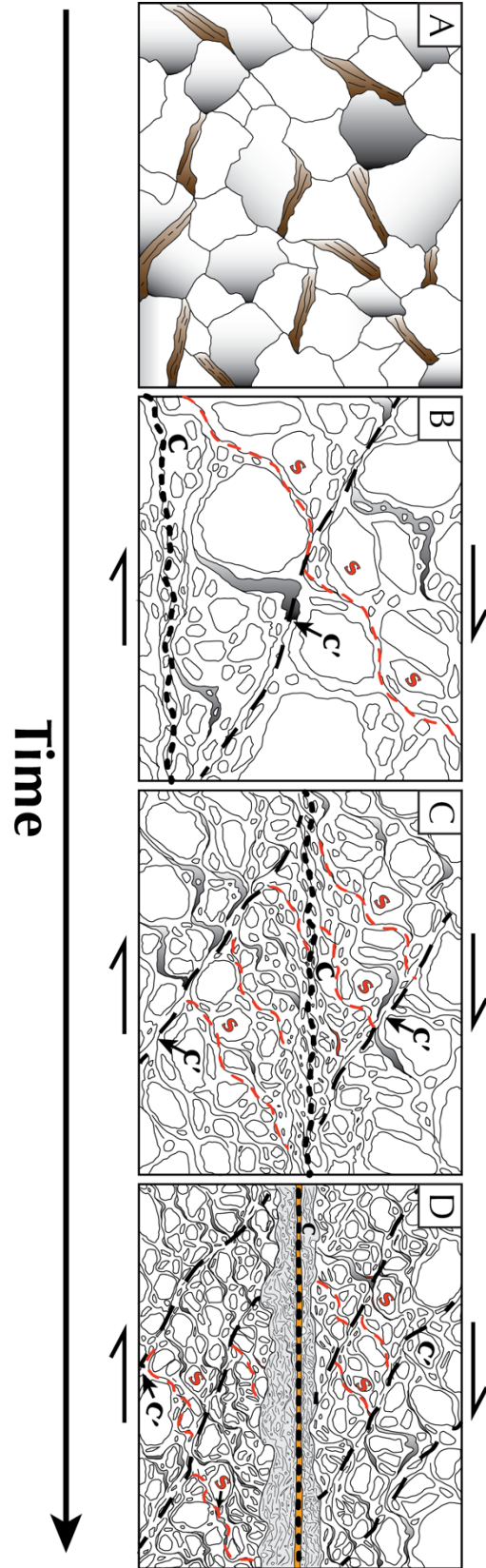
548

549 In addition to describing fault surface geometry via fractal descriptors (H_{per} , H_{par} , C_{par} , C_{per}),
550 this work includes multiscale analyses (MSA) on the height distribution of fault surfaces. Our
551 results suggest the kurtosis and skewness of such distributions deviate from Gaussian with a
552 noticeable dependence on the scale of observation, which contrast to some of the models used in
553 earthquake simulations that typically assume faults as Gaussian self-affine rough surfaces (e.g.,
554 (Cattania & Segall, 2021; Graves & Pitarka, 2016). The latter has important implications on our
555 understanding of the role of geometry in faulting processes, as studies on the contact behavior of
556 non-Gaussian surfaces have reported that roughness parameters skewness and kurtosis correlate to
557 noticeable effects on tribological properties such as: friction, wear, mean asperity pressure, and
558 contact area (Ghosh & Sadeghi, 2015; Gu et al., 2021; Kim et al., 2006; Kotwal & Bhushan, 1996;
559 McCool, 1992; Sedláček et al., 2012; Tayebi & Polycarpou, 2004; Tomota et al., 2019; W.-Z.
560 Wang et al., 2006; Yan et al., 2014; S. Zhang et al., 2014) and fluid transport properties (M. Wang
561 et al., 2016). Thus, further measurements of fault surfaces that also characterizes the distribution
562 of their heights in addition to their fractality seem crucial for more accurate representations of fault
563 roughness in models that explore the role of geometry on seismic slip.

564

565 While this simplification of fault zones into self-affine rough surfaces is useful for making
566 educated predictions of fault surface geometry at scales and locations not accessible with the
567 current technology (subsurface faults), it is worth noting that wear and therefore slip on a fault
568 cannot be entirely explained by two rough surfaces sliding past each other. Firstly, microstructural
569 observations near single fault surfaces have reported the presence of a discrete zone that
570 concentrates strain and wear comprising extremely comminuted layers with an abundance of
571 nanoparticles and/or other types of tribofilms, within the PSZ and PSS (Ault et al., 2019; De Paola,
572 2013; Dor & Reches, 2005; Goldberg et al., 2016; Heesakkers et al., 2011; Houser et al., 2021;
573 Kuo et al., 2016; Ohl et al., 2020; Otsubo et al., 2013; Pec et al., 2016; Power & Tullis, 1989;
574 Rowe et al., 2019; Shervais & Kirkpatrick, 2016; Siman-Tov et al., 2013, 2015; Taylor et al., 2021;
575 Tisato et al., 2012; Verberne et al., 2014, 2019; Viti et al., 2016), suggesting that individual fault
576 surface evolution and wear could be better modeled by what is known in tribology as third-body
577 wear (Boneh et al., 2014; Boneh & Reches, 2018; Brodsky et al., 2020; Milanese et al., 2019).
578 More importantly, however, geologic and experimental observations from the submillimeter to
579 kilometers scale indicate that fault zones involve the interaction several structures, with multiple
580 anastomosing fault strands occasionally crosscutting each other (Faulkner et al., 2003; Rowe et al.,
581 2018; Shervais & Kirkpatrick, 2016; Swanson, 1988; Torabi et al., 2020, 2021). For instance,
582 observations of individual natural slickensides and their respective host rocks reveal an intricate
583 set of structures that document progressive localization of strain into what eventually become
584 multiple principal slip surfaces on which subsequent sliding takes place. Specifically, most
585 samples exhibited foliated cataclasites with S-C-like fabrics, with clasts progressively becoming
586 finer toward the C-plane-parallel principal slip surfaces as documented in Fig.9, similar to the
587 structures reported along the PSS of numerous other fault zones (Berthé et al., 1979; Hippert,

588 1999; Jordan, 1987; Kirkpatrick & Brodsky, 2014; Y.-J. Lee, 1991; A. Lin, 2001; S. Lin et al.,
589 2007; S. Lin & Williams, 1992; Nakamura & Nagahama, 2002; Ortega-Arroyo, 2017). Such
590 observations suggest that development of the PSS is preceded by formation of progressively
591 mechanically weaker zones along which strain is further localized. A simple sequential model is
592 proposed in Fig. 13 based on the observations from natural slickenside samples, analogue
593 experiments with no pre-cut fault surfaces (Will & Wilson, 1989; C. J. L. Wilson & Will, 1990)
594 and numerical modeling (Finch et al., 2020). Therefore, in our interpretation the exposed slip
595 surfaces are the end product of fault slip and wear on fault zone and not the initial conditions on
596 which slip initiate.



598 **Figure 13.** Schematic sequential model of slickenside development. A) Initial undeformed rock.
599 B) S-C-C' fabrics start developing at low -intermediate strain levels. Note S-foliation (red-dashed
600 lines) is defined by asymmetrical clast and clast aggregates with their tails oriented at about 45° to
601 the C-surface (black-dotted lines), whereas C'-shear bands appear oblique orientations (black-
602 dashed lines). C) As shearing continues more S-C' fabrics propagate throughout the sample and
603 create rheologically weaker regions via grain size reduction that preferentially rotate towards C-
604 planes. D) Strain further localizes along the C-planes in the form of finely comminuted material
605 observed in the PSZ (grey) and PSS (yellow)
606

607 At low to intermediate strain, deformation is accommodated via incremental development of
608 oriented fabrics along S-C structures (Will & Wilson, 1989; C. J. L. Wilson & Will, 1990). At
609 higher strains, passive rotation of S-planes into C-planes becomes a more efficient way to
610 accommodate strain over creation of new planes, (Berthé et al., 1979; Finch et al., 2020; Hippertt,
611 1999; Jordan, 1987), which create rheologically weaker regions that accommodate higher strain
612 rates (Finch et al., 2020) and can progressively link with each other to form through going shear
613 zones (Finch et al., 2020; Pec et al., 2016; Will & Wilson, 1989; C. J. L. Wilson & Will, 1990),
614 akin to the process zone suggested by (Cox & Scholz, 1988). The development of these localized
615 shear zones also facilitates infiltration of fluids, as seen in the ubiquitous concentration of
616 secondary minerals and/or alteration products (mainly Fe-ox) along the PSZ and PSS, Figs. 8-11,
617 that likely cause further weakening and slip due to metasomatic reactions and pore pressure effects.
618 The latter suggests an extreme degree of strain localization, where most of the deformation is
619 accommodated by extreme comminution along thin kinematically favorable regions, generally a
620 few tens of microns thick, as documented in Figs. 8-10.

621 To better characterize the extreme comminution processes affecting our samples we performed
622 grain size analyses. Interestingly, the way the grain sizes are distributed appears to vary between
623 the andesite and the quartzite sample. For instance, the slickenside within the quartzite shows a
624 GSD that can be described with a single D value for over six orders of magnitude, whereas the
625 andesite GSD has a break in slope near $d_k \approx 2 \mu\text{m}$, Fig. 12. Grain size measurements from other
626 polymineralic natural and experimental fault rocks have also reported a break in the slope of their
627 GSD at similar critical grain sizes d_k that suggest a change in the dominant comminution
628 mechanisms with attrition and shearing becoming more important at values lower than d_k , usually
629 attributed to the grinding limit (Billi & Storti, 2004; F. M. Chester et al., 1993; J. S. Chester et al.,

2005; Keulen et al., 2007). Our quartzite sample does not exhibit this transition and is in contrast to what Keulen et al., (2007) reported for quartz grains in other polymineralic gouges. There could be multiple explanations for the discrepancies at these scales. Firstly, the difference could be related to different breakage mechanisms at sub-micron scale associated to the parent mineralogy (Knieke et al., 2011), as the observations reported in Keulen et al., (2007) were done on granitoid lithologies and ours on quartzite and andesite. Moreover, the break in slope observed in the andesite GSD could be related to changes in material properties likely caused by mechanochemical and/or tribochemical reactions acting along the friction zone, PSS, as the d_k appears at the transition where their grain sizes overlap between the PSZ and PSS, (Knieke, 2012; Knieke et al., 2011; Romeis et al., 2016). It is possible that partial mechanical amorphization is among some of the reactions occurring within the PSS, which could help explain the distinct textures observed along the PSS and its GSD. For instance, the dense portion of the PSS, Fig 10B,E,F , exhibits similar textures to those observed along the silica layer within the slickensides studied by Taylor et al., (2021), wherein Fe-ox nanorods are embedded in a partially amorphous matrix, while the “wispy” microporous matrix, observed in Fig. 10A, resembles the textures reported from hydrothermally altered quenched frictional melts in (Fondriest et al., 2020) likely representing portions that have undergone more advanced hydrothermal alteration with formation of clay minerals, (e.g., Fe-smectite). Furthermore, observations of coeval amorphous and nanocrystalline material are not uncommon along high strain frictional interfaces and have been widely reported along natural fault surfaces (Ault et al., 2019; Houser et al., 2021; Kirkpatrick et al., 2013; Kuo et al., 2016; Ohl et al., 2020; Verberne et al., 2014, 2019; Viti et al., 2016), rock deformation experiments (Kaneki et al., 2020; Marti et al., 2020; Pec et al., 2012, 2016; Pec & Al Nasser, 2021; Toy et al., 2017), and deformation of engineering materials (Han et al., 2012; Viat et al., 2017; Y. S. Zhang et al., 2014;

653 Zhao et al., 2016), indicating that both nanocrystalline and amorphous material are common
654 products during frictional wear processes regardless of the parent material, and an important
655 component to consider when studying rheology of faults. Nanocrystalline fault rocks are inherently
656 weaker than their microcrystalline counterparts and therefore can form in-situ weak layers along
657 which strain further localizes (Sun and Pec 2021).

658 Alternatively, both GSD's could also represent different stages in the comminution process as
659 recent studies in confined comminution of granular materials using a simple Discrete Element
660 Models (DEM) and Apollonian gasket models suggest that the GSD continuously shifts as the
661 porosity is reduced until it reaches an ultimate power law that also determines the ultimate contact
662 force distribution (Ben-Nun et al., 2010). Based on the microstructure of each sample it is possible
663 that the observed changes relate to different degrees of comminution. Similarly, Knieke et al.
664 (2009) work on ultrafine particle (nm-range) production with stirred media mills on a variety of
665 different materials shows that the ultimate size that a particle can be broken into, i.e., grinding
666 limit, depends on a multitude of variables including stressing types, the material of the particles to
667 be milled as well as the size and material of the milling particles, and solvents (e.g., hydrous fluids).
668 Thus, the ultimate particle distribution observed along comminuted rocks could reflect the
669 conditions during grinding.

670

671

672

673

674 **5 Summary and Conclusions**

675 We investigated the surface roughness and associated microstructures of natural
676 slickenside samples from three different fault systems hosted in andesite, quartzite and mylonitic
677 meta-sedimentary lithologies. We found that in addition to exhibiting the usually reported self-
678 affine roughness, with mean $H_{par}=0.53 \pm 0.07$ and $H_{per}=0.60 \pm 0.10$, all surfaces exhibited non-
679 Gaussian height distributions with noticeable scale-dependence on their S_{kur} and S_{sk} roughness
680 parameters. While our dataset is limited to the shorter length scales associated with fault surface
681 roughness, further studies at a wider range of scales could help constrain the type of height
682 distributions common to natural faults. Moreover, our microstructural analyses suggest such
683 surfaces are likely the product of progressive strain localization and partitioning along regions with
684 high degree of fabric development (S-C-C'- fabrics) that culminate in multiple principal slip zones
685 throughout the samples identified by a sharp decrease in clast size and thin ($\leq 100 \mu\text{m}$) principal
686 slip surfaces wherein nanosized particles are abundant along with other tribofilms and reaction
687 products. The prevalence of nanoparticles observed within fault zones regardless of lithology or
688 tectonic setting urges the need to investigate the effect of nanogranular material on the rheological
689 and frictional properties of faults. In this light, a re-visiting of the energy budget of faulting seems
690 necessary to account for the interaction between various structures (present even along individual
691 slip surfaces) and the work done to decrease the grain sizes to nanometers. Partitioning of energy
692 between heat, grain breakage, intracrystalline deformation, amorphization, and seismic wave
693 radiation will ultimately influence how much energy goes into heating (Bestmann et al., 2011;
694 Knieke et al., 2011; Ranganathan et al., 2021; Rosakis et al., 2000; B. Wilson et al., 2005). Heating
695 of fault zones and the associated microstructural changes present the best opportunity to

696 distinguish between fault segments that underwent rapid slip from fault segments that crept at slow
697 rates (Rowe & Griffith, 2015 and references therein).

698

699 **6 Acknowledgments**

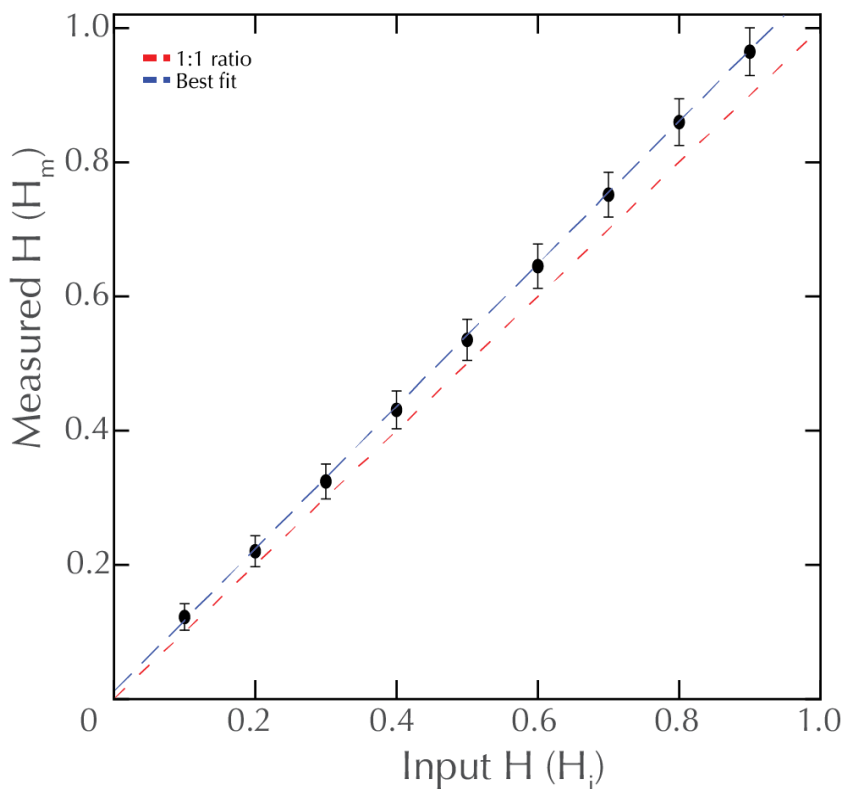
700 Funding for the CORD technician support from NSF # 1833478 and funding by the J.H. and E.V.
701 Wade Fund from MIT's research support committee is gratefully acknowledged. We would also
702 like to acknowledge the staff at the Materials Research Science and Engineering Centers at the
703 Massachusetts Institute of Technology for their help with their ZEISS Merlin HR-SEM.

704 We would also like to thank Christie Rowe and McGill University, who allowed us to join their
705 2019 field course and collect the Waterman Hill samples. The MIT-EAPS 2020 field course for
706 allowing us to collect the Big Piute samples, and Juan Ignacio Arroyo Verástegui, who helped me
707 collect the sample from Falla de Plan de los Plátanos.

708

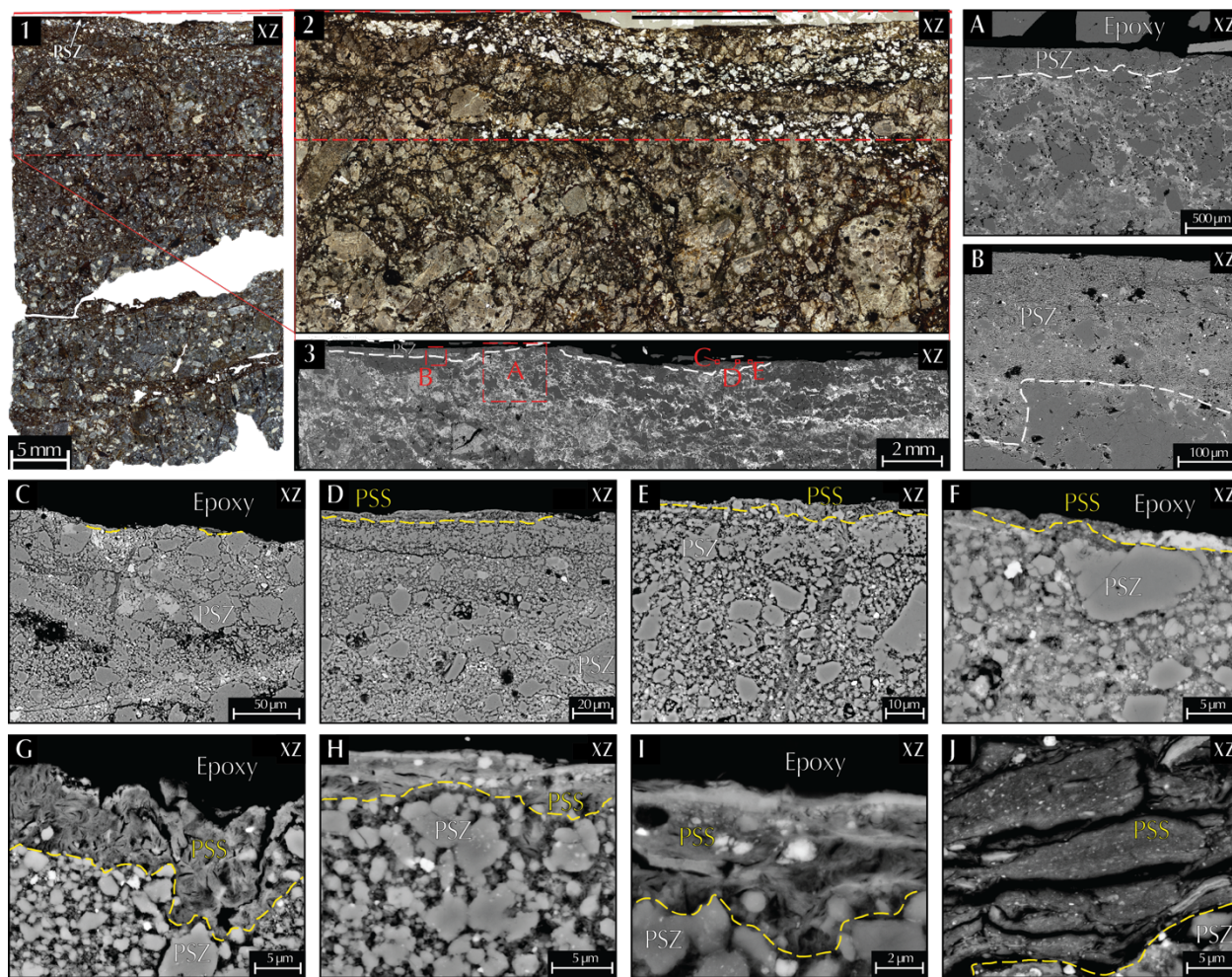
709 **7 Appendix**

710 The accuracy of the signal processing technique was assessed by recording the difference between
711 the “input” Hurst exponents of randomly generated synthetic isotropic self-affine surfaces using
712 the code provided in Candela et al. (2009) and the “output” recovered with our methods. For each
713 value of the input Hurst exponent, we analyzed a set of 1000 synthetically generated surfaces as
714 presented in Fig. A1. We further assessed our method by analyzing surface data from the Corona
715 Heights fault surface samples from Thom et al. (2017). The average Hurst exponents of the Corona
716 Heights Fault slickenside samples corresponded to 0.72 ± 0.11 and 0.78 ± 0.09 for the parallel
717 and perpendicular orientations, respectively. However, when the data in both directions are taken
718 into account, we obtained 0.75 ± 0.10 , which agrees with the value found by Thom et al. (2017).



719

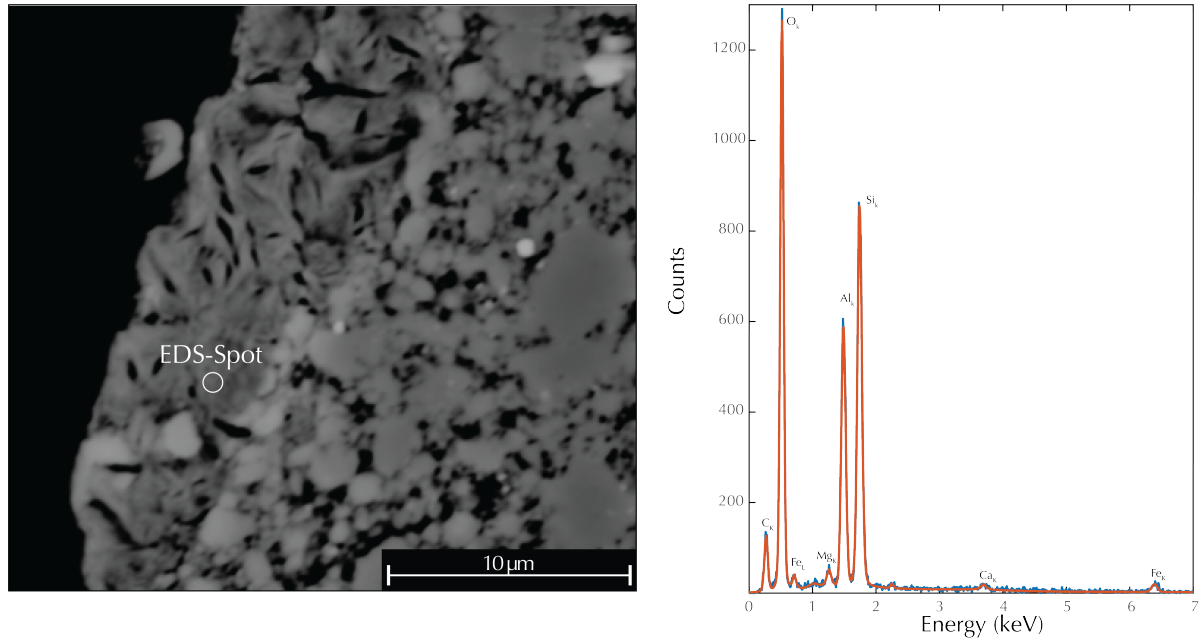
720 **Figure A1.** Calibration of PSD method for calculating the Hurst exponent (H). Note that the
 721 measured Hurst exponent (H_m) does not follow a one-to-one ratio (red). Instead, it has a linear best
 722 fit of the form $H_m = 1.065 H_i + 0.006$ with a coefficient of determination $R^2 = 0.999$.



723
 724 **Figure A2.** Set of images at progressively higher magnifications used in the GSD determination
 725 of andesite hosted slickenside. See text for details.

726

727



728
729
730
731

Figure A3. EDS-spectrum of “wispy” PSS from andesite hosted slickensides.

732 **8 Data Availability Statement**

733 Data reported here are publicly available at Zenodo Repository at:
734 <https://doi.org/10.5281/zenodo.6558132> (SEM and petrographic photomicrographs),
735 <https://doi.org/10.5281/zenodo.5167913> (surface roughness data), and
736 <https://doi.org/10.5281/zenodo.6558649> (grain size distribution data) under a Creative Commons
737 Attribution 4.0 International Public License.

738 **9 References**

739
740 Ault, A. K., Jensen, J. L., McDermott, R. G., Shen, F.-A., & Van Devenner, B. R. (2019).
741 Nanoscale evidence for temperature-induced transient rheology and postseismic fault
742 healing. *Geology*, 47(12), 1203–1207. <https://doi.org/10.1130/G46317.1>
743 Ben-Nun, O., Einav, I., & Tordesillas, A. (2010). Force attractor in confined comminution of
744 granular materials. *Physical Review Letters*, 104(10), 108001.

745 <https://doi.org/10.1103/PhysRevLett.104.108001>

746 Ben-Zion, Y., & Rice, J. R. (1997). Dynamic simulations of slip on a smooth fault in an elastic
747 solid. *Journal of Geophysical Research*, *102*(B8), 17771–17784.
748 <https://doi.org/10.1029/97jb01341>

749 Berthé, D., Choukroune, P., & Jegouzo, P. (1979). Orthogneiss, mylonite and non coaxial
750 deformation of granites: the example of the South Armorican Shear Zone. *Journal of*
751 *Structural Geology*, *1*(1), 31–42. [https://doi.org/10.1016/0191-8141\(79\)90019-1](https://doi.org/10.1016/0191-8141(79)90019-1)

752 Bestmann, M., Pennacchioni, G., Frank, G., Göken, M., & de Wall, H. (2011). Pseudotachylyte
753 in muscovite-bearing quartzite: Coseismic friction-induced melting and plastic
754 deformation of quartz. *Journal of Structural Geology*, *33*(2), 169–186.
755 <https://doi.org/10.1016/j.jsg.2010.10.009>

756 Bhushan, B. (2013). *Introduction to Tribology*. John Wiley & Sons. Retrieved from
757 <https://play.google.com/store/books/details?id=b0nhJrqsoZ0C>

758 Billi, A., & Storti, F. (2004). Fractal distribution of particle size in carbonate cataclastic rocks
759 from the core of a regional strike-slip fault zone. *Tectonophysics*, *384*(1), 115–128.
760 <https://doi.org/10.1016/j.tecto.2004.03.015>

761 Bistacchi, A., Griffith, W. A., Smith, S. A. F., Di Toro, G., Jones, R., & Nielsen, S. (2011). Fault
762 Roughness at Seismogenic Depths from LIDAR and Photogrammetric Analysis. *Pure*
763 *and Applied Geophysics*, *168*(12), 2345–2363. [https://doi.org/10.1007/s00024-011-0301-](https://doi.org/10.1007/s00024-011-0301-7)
764 [7](https://doi.org/10.1007/s00024-011-0301-7)

765 Boneh, Y., & Reches, Z. (2018). Geotribology - Friction, wear, and lubrication of faults.
766 *Tectonophysics*, *733*, 171–181. <https://doi.org/10.1016/j.tecto.2017.11.022>

767 Boneh, Y., Chang, J. C., Lockner, D. A., & Reches, Z. (2014). Evolution of Wear and Friction

768 Along Experimental Faults. *Pure and Applied Geophysics*, 171(11), 3125–3141.
769 <https://doi.org/10.1007/s00024-014-0801-3>

770 Bowden, F. P., Tabor, D., & Taylor, G. I. (1939). The area of contact between stationary and
771 moving surfaces. *Proceedings of the Royal Society of London. Series A, Mathematical*
772 *and Physical Sciences*, 169(938), 391–413. <https://doi.org/10.1098/rspa.1939.0005>

773 Brodsky, E. E., Kirkpatrick, J. D., & Candela, T. (2016). Constraints from fault roughness on the
774 scale-dependent strength of rocks. *Geology*, 44(1), 19–22.
775 <https://doi.org/10.1130/G37206.1>

776 Brodsky, E. E., McLaskey, G. C., & Ke, C.-Y. (2020). Groove generation and coalescence on a
777 large-scale laboratory fault. *AGU Advances*, 1(4). <https://doi.org/10.1029/2020av000184>

778 Brown, C. A., Hansen, H. N., Jiang, X. J., Blateyron, F., Berglund, J., Senin, N., et al. (2018).
779 Multiscale analyses and characterizations of surface topographies. *CIRP Annals*, 67(2),
780 839–862. <https://doi.org/10.1016/j.cirp.2018.06.001>

781 Brown, S. R., & Scholz, C. H. (1985). Broad bandwidth study of the topography of natural rock
782 surfaces. *Journal of Geophysical Research*, 90(B14), 12575.
783 <https://doi.org/10.1029/jb090ib14p12575>

784 Bruhat, L., Klinger, Y., Vallage, A., & Dunham, E. M. (2020). Influence of fault roughness on
785 surface displacement: from numerical simulations to coseismic slip distributions.
786 *Geophysical Journal International*, 220(3), 1857–1877.
787 <https://doi.org/10.1093/gji/ggz545>

788 Caine, J. S., Evans, J. P., & Forster, C. B. (1996). Fault zone architecture and permeability
789 structure. *Geology*, 24(11), 1025–1028. [https://doi.org/10.1130/0091-](https://doi.org/10.1130/0091-7613(1996)024<1025:FZAAPS>2.3.CO;2)
790 [7613\(1996\)024<1025:FZAAPS>2.3.CO;2](https://doi.org/10.1130/0091-7613(1996)024<1025:FZAAPS>2.3.CO;2)

791 Candela, T., Renard, F., Bouchon, M., Brouste, A., Marsan, D., Schmittbuhl, J., & Voisin, C.
792 (2009). Characterization of Fault Roughness at Various Scales: Implications of Three-
793 Dimensional High Resolution Topography Measurements. *Pure and Applied Geophysics*,
794 *166*(10), 1817–1851. <https://doi.org/10.1007/s00024-009-0521-2>

795 Candela, T., Renard, F., Klinger, Y., Mair, K., Schmittbuhl, J., & Brodsky, E. E. (2012).
796 Roughness of fault surfaces over nine decades of length scales. *Journal of Geophysical*
797 *Research*, *117*(B8). <https://doi.org/10.1029/2011jb009041>

798 Cattania, C., & Segall, P. (2021). Precursory slow slip and foreshocks on rough faults. *Journal of*
799 *Geophysical Research, [Solid Earth]*, *126*(4). <https://doi.org/10.1029/2020jb020430>

800 Chen, J., Verberne, B. A., & Niemeijer, A. R. (2020). Flow-to-Friction Transition in Simulated
801 Calcite Gouge: Experiments and Microphysical Modeling. *Journal of Geophysical*
802 *Research, [Solid Earth]*, *125*(11), e2020JB019970.
803 <https://doi.org/10.1029/2020JB019970>

804 Chen, X., Madden, A. S., Bickmore, B. R., & Reches, Z. (2013). Dynamic weakening by
805 nanoscale smoothing during high-velocity fault slip. *Geology*, *41*(7), 739–742.
806 <https://doi.org/10.1130/G34169.1>

807 Chester, F. M., & Logan, J. M. (1986). Implications for mechanical properties of brittle faults
808 from observations of the Punchbowl fault zone, California. *Pure and Applied Geophysics*,
809 *124*(1), 79–106. <https://doi.org/10.1007/BF00875720>

810 Chester, F. M., Friedman, M., & Logan, J. M. (1985). Foliated cataclasites. *Tectonophysics*,
811 *111*(1), 139–146. [https://doi.org/10.1016/0040-1951\(85\)90071-X](https://doi.org/10.1016/0040-1951(85)90071-X)

812 Chester, F. M., Evans, J. P., & Biegel, R. L. (1993). Internal structure and weakening
813 mechanisms of the San Andreas Fault. *Journal of Geophysical Research*, *98*(B1), 771–

814 786. <https://doi.org/10.1029/92jb01866>

815 Chester, J. S., Chester, F. M., & Kronenberg, A. K. (2005). Fracture surface energy of the
816 Punchbowl fault, San Andreas system. *Nature*, *437*(7055), 133–136.
817 <https://doi.org/10.1038/nature03942>

818 Chu, S. X., Tsai, V. C., Trugman, D. T., & Hirth, G. (2021). Fault interactions enhance high-
819 frequency earthquake radiation. *Geophysical Research Letters*, *48*(20).
820 <https://doi.org/10.1029/2021gl095271>

821 Cox, S. J. D., & Scholz, C. H. (1988). On the formation and growth of faults: an experimental
822 study. *Journal of Structural Geology*. Retrieved from
823 <https://www.sciencedirect.com/science/article/pii/0191814188900193>

824 De la Teja Segura, M. Á., & Roque Ayala, A. (2007). Carta Geológica-Minera Autlán de
825 Navarro E13-B12 Jalisco. (S. G. Mexicano, Ed.). Pachuca, HGO, Mexico : Servicio
826 Geológico Mexicano. Retrieved from
827 http://mapserver.sgm.gob.mx/Cartas_Online/geologia/956_E13-B12_GM.pdf

828 De Paola, N. (2013). Nano-powder coating can make fault surfaces smooth and shiny:
829 implications for fault mechanics? *Geology*, *41*(6), 719–720.
830 <https://doi.org/10.1130/focus062013.1>

831 Di Toro, G., Han, R., Hirose, T., De Paola, N., Nielsen, S., Mizoguchi, K., et al. (2011). Fault
832 lubrication during earthquakes. *Nature*, *471*(7339), 494–498.
833 <https://doi.org/10.1038/nature09838>

834 Dieterich, J. H., & Kilgore, B. D. (1996). Imaging surface contacts: power law contact
835 distributions and contact stresses in quartz, calcite, glass and acrylic plastic.
836 *Tectonophysics*, *256*(1), 219–239. [https://doi.org/10.1016/0040-1951\(95\)00165-4](https://doi.org/10.1016/0040-1951(95)00165-4)

837 Doblas, M. (1998). Slickenside kinematic indicators. *Tectonophysics*, 295(1), 187–197.
838 [https://doi.org/10.1016/S0040-1951\(98\)00120-6](https://doi.org/10.1016/S0040-1951(98)00120-6)

839 Dor, O., & Reches, Z. (2005). *Analysis of Fault Zones Associated with Large Earthquakes in*
840 *South African Gold Mines*. Earth Sciences Institute, Hebrew University, Jerusalem,
841 Israel. Retrieved from http://earthquakes.ou.edu/nelsam/fault_zones.pdf

842 Evans, J. P., Prante, M. R., Janecke, S. U., & Ault, A. K. (2014). Hot faults: Iridescent slip
843 surfaces with metallic luster document high-temperature ancient seismicity in the
844 Wasatch fault zone, Utah, USA. Retrieved from
845 <https://pubs.geoscienceworld.org/gsa/geology/article-abstract/42/7/623/131640>

846 Faulkner, D. R., Lewis, A. C., & Rutter, E. H. (2003). On the internal structure and mechanics of
847 large strike-slip fault zones: field observations of the Carboneras fault in southeastern
848 Spain. *Tectonophysics*, 367(3), 235–251. [https://doi.org/10.1016/S0040-1951\(03\)00134-3](https://doi.org/10.1016/S0040-1951(03)00134-3)

849 Faulkner, D. R., Jackson, C. A. L., Lunn, R. J., Schlische, R. W., Shipton, Z. K., Wibberley, C.
850 A. J., & Withjack, M. O. (2010). A review of recent developments concerning the
851 structure, mechanics and fluid flow properties of fault zones. *Journal of Structural*
852 *Geology*, 32(11), 1557–1575. <https://doi.org/10.1016/j.jsg.2010.06.009>

853 Faulkner, D. R., Mitchell, T. M., Jensen, E., & Cembrano, J. (2011). Scaling of fault damage
854 zones with displacement and the implications for fault growth processes. *Journal of*
855 *Geophysical Research*, 116(B5). <https://doi.org/10.1029/2010jb007788>

856 Ferrari, L., Pasquaré, G., Venegas-Salgado, S., & Romero-Rios, F. (2000). Geology of the
857 western Mexican Volcanic Belt and adjacent Sierra Madre Occidental and Jalisco Block.
858 In *Cenozoic tectonics and volcanism of Mexico* (pp. 65–83). Geological Society of
859 America. <https://doi.org/10.1130/0-8137-2334-5.65>

860 Finch, M. A., Bons, P. D., Steinbach, F., Grier, A., Llorens, M.-G., Gomez-Rivas, E., et al.
861 (2020). The ephemeral development of C' shear bands: A numerical modelling approach.
862 *Journal of Structural Geology*, 139, 104091. <https://doi.org/10.1016/j.jsg.2020.104091>

863 Fletcher, J. M., & Karlstrom, K. E. (1990). Late Cretaceous ductile deformation, metamorphism
864 and plutonism in the Piute Mountains, eastern Mojave Desert. *Journal of Geophysical*
865 *Research*, 95(B1), 487. <https://doi.org/10.1029/jb095ib01p00487>

866 Fletcher, J. M., Bendixen, J., Fillmore, R., Walker, J. D., Glazner, A. F., & Bartley, J. M. (1999).
867 Geology of the Mitchel Range and Waterman Hills, San Bernardino County, California.
868 Geological society of America. <https://doi.org/10.1130/1999-fletcher-watermanhills>

869 Fleuty, M. J. (1975). Slickensides and slickenlines. *Geological Magazine*, 112(3), 319–322.
870 <https://doi.org/10.1017/S0016756800047087>

871 Fondriest, M., Mecklenburgh, J., Passelegue, F. X., Artioli, G., Nestola, F., Spagnuolo, E., et al.
872 (2020). Pseudotachylyte alteration and the rapid fade of earthquake scars from the
873 geological record. *Geophysical Research Letters*, 47(22).
874 <https://doi.org/10.1029/2020gl090020>

875 Gadelmawla, E. S., Koura, M. M., Maksoud, T. M. A., Elewa, I. M., & Soliman, H. H. (2002).
876 Roughness parameters. *Journal of Materials Processing Technology*, 123(1), 133–145.
877 [https://doi.org/10.1016/S0924-0136\(02\)00060-2](https://doi.org/10.1016/S0924-0136(02)00060-2)

878 Ghosh, A., & Sadeghi, F. (2015). A novel approach to model effects of surface roughness
879 parameters on wear. *Wear: An International Journal on the Science and Technology of*
880 *Friction Lubrication and Wear*, 338–339, 73–94.
881 <https://doi.org/10.1016/j.wear.2015.04.022>

882 Glazner, A. F., & Mills, R. D. (2012). Interpreting two-dimensional cuts through broken

883 geologic objects: Fractal and non-fractal size distributions. *Geosphere*, 8(4), 902–914.
884 <https://doi.org/10.1130/GES00731.1>

885 Glazner, A. F., Bartley, J. M., & Douglas Walker, J. (1989). Magnitude and significance of
886 Miocene crustal extension in the central Mojave Desert, California. *Geology*, 17(1), 50–
887 53. [https://doi.org/10.1130/0091-7613\(1989\)017<0050:MASOMC>2.3.CO;2](https://doi.org/10.1130/0091-7613(1989)017<0050:MASOMC>2.3.CO;2)

888 Gold, P. O., Behr, W. M., Fletcher, J. M., Rockwell, T. K., & Figueiredo, P. M. (2020). Time-
889 invariant late Quaternary slip rates along the Agua Blanca fault, northern Baja California,
890 Mexico. *Tectonics*, 39(9). <https://doi.org/10.1029/2019tc005788>

891 Goldberg, R., Siman-Tov, S., & Emmanuel, S. (2016). Weathering resistance of carbonate fault
892 mirrors promotes rupture localization. *Geophysical Research Letters*.
893 <https://doi.org/10.1002/2016gl067788>

894 Graves, R., & Pitarka, A. (2016). Kinematic Ground-Motion Simulations on Rough Faults
895 Including Effects of 3D Stochastic Velocity Perturbations Kinematic Ground-Motion
896 Simulations on Rough Faults. *Bulletin of the Seismological Society of America*, 106(5),
897 2136–2153. <https://doi.org/10.1785/0120160088>

898 Gu, C., Meng, X., Wang, S., & Ding, X. (2021). Study on the mutual influence of surface
899 roughness and texture features of rough-textured surfaces on the tribological properties.
900 *Proceedings of the Institution of Mechanical Engineers, Part J: Journal of Engineering*
901 *Tribology*, 235(2), 256–273. <https://doi.org/10.1177/1350650120940211>

902 Han, S., Zhao, L., Jiang, Q., & Lian, J. (2012). Deformation-induced localized solid-state
903 amorphization in nanocrystalline nickel. *Scientific Reports*, 2, 493.
904 <https://doi.org/10.1038/srep00493>

905 Harbord, C. W. A., Nielsen, S. B., De Paola, N., & Holdsworth, R. E. (2017). Earthquake

906 nucleation on rough faults. *Geology*, 45(10), 931–934. <https://doi.org/10.1130/G39181.1>

907 Heesakkers, V., Murphy, S., & Reches, Z. (2011). Earthquake Rupture at Focal Depth, Part I:
908 Structure and Rupture of the Pretorius Fault, TauTona Mine, South Africa. *Pure and*
909 *Applied Geophysics*, 168(12), 2395–2425. <https://doi.org/10.1007/s00024-011-0354-7>

910 Heilbronner, R., & Barrett, S. (2014). Fractal Grain Size Distributions. In R. Heilbronner & S.
911 Barrett (Eds.), *Image Analysis in Earth Sciences: Microstructures and Textures of Earth*
912 *Materials* (pp. 225–249). Berlin, Heidelberg: Springer Berlin Heidelberg.
913 https://doi.org/10.1007/978-3-642-10343-8_13

914 Hippertt, J. (1999). Are S–C structures, duplexes and conjugate shear zones different
915 manifestations of the same scale-invariant phenomenon? *Journal of Structural Geology*,
916 21(8), 975–984. [https://doi.org/10.1016/S0191-8141\(99\)00047-4](https://doi.org/10.1016/S0191-8141(99)00047-4)

917 Houser, L. M., Ault, A. K., Newell, D. L., Evans, J. P., Shen, F.-A., & Van Devener, B. R.
918 (2021). Nanoscale textural and chemical evolution of silica fault mirrors in the Wasatch
919 fault damage zone, Utah, USA. *Geochemistry, Geophysics, Geosystems*, 22(3).
920 <https://doi.org/10.1029/2020gc009368>

921 Jacobs, T. D. B., Junge, T., & Pastewka, L. (2017). Quantitative characterization of surface
922 topography using spectral analysis. *Surface Topography: Metrology and Properties*, 5(1),
923 013001. <https://doi.org/10.1088/2051-672X/aa51f8>

924 Jordan, P. G. (1987). The deformational behaviour of bimineralic limestone-halite aggregates.
925 *Tectonophysics*, 135(1), 185–197. [https://doi.org/10.1016/0040-1951\(87\)90160-0](https://doi.org/10.1016/0040-1951(87)90160-0)

926 Kaneki, S., Oohashi, K., Hirono, T., & Noda, H. (2020). Mechanical amorphization of synthetic
927 fault gouges during rotary-shear friction experiments at subseismic to seismic slip
928 velocities. *Journal of Geophysical Research, [Solid Earth]*, 125(10).

929 <https://doi.org/10.1029/2020jb019956>

930 Kearse, J., Kaneko, Y., Little, T., & Van Dissen, R. (2019). Curved slickenlines preserve
931 direction of rupture propagation. *Geology*, *47*(9), 838–842.
932 <https://doi.org/10.1130/G46563.1>

933 Keulen, N., Heilbronner, R., Stünitz, H., Boullier, A.-M., & Ito, H. (2007). Grain size
934 distributions of fault rocks: A comparison between experimentally and naturally
935 deformed granitoids. *Journal of Structural Geology*, *29*(8), 1282–1300.
936 <https://doi.org/10.1016/j.jsg.2007.04.003>

937 Keulen, N., Stünitz, H., & Heilbronner, R. (2008). Healing microstructures of experimental and
938 natural fault gouge. *Journal of Geophysical Research*, *113*(B6).
939 <https://doi.org/10.1029/2007jb005039>

940 Kim, T. W., Bhushan, B., & Cho, Y. J. (2006). The contact behavior of elastic/plastic non-
941 Gaussian rough surfaces. *Tribology Letters*, *22*(1), 1. [https://doi.org/10.1007/s11249-006-](https://doi.org/10.1007/s11249-006-9036-5)
942 [9036-5](https://doi.org/10.1007/s11249-006-9036-5)

943 Kirkpatrick, J. D., & Brodsky, E. E. (2014). Slickenline orientations as a record of fault rock
944 rheology. *Earth and Planetary Science Letters*, *408*, 24–34.
945 <https://doi.org/10.1016/j.epsl.2014.09.040>

946 Kirkpatrick, J. D., Rowe, C. D., White, J. C., & Brodsky, E. E. (2013). Silica gel formation
947 during fault slip: Evidence from the rock record. *Geology*, *41*(9), 1015–1018.
948 <https://doi.org/10.1130/G34483.1>

949 Knieke, C. (2012). *Fracture at the Nanoscale and the Limit of Grinding: Partikelbruch Im*
950 *Nanometerbereich und Die Grenze Der Echtzerkleinerung*. Cuvillier.

951 Knieke, C., Romeis, S., & Peukert, W. (2011). Influence of process parameters on breakage

952 kinetics and grinding limit at the nanoscale. *AIChE Journal. American Institute of*
953 *Chemical Engineers*, 57(7), 1751–1758. <https://doi.org/10.1002/aic.12408>

954 Kotwal, C. A., & Bhushan, B. (1996). Contact Analysis of Non-Gaussian Surfaces for Minimum
955 Static and Kinetic Friction and Wear. *Tribology Transactions*, 39(4), 890–898.
956 <https://doi.org/10.1080/10402009608983609>

957 Kuo, L.-W., Song, S.-R., Suppe, J., & Yeh, E.-C. (2016). Fault mirrors in seismically active fault
958 zones: A fossil of small earthquakes at shallow depths. *Geophysical Research Letters*,
959 43(5), 1950–1959. <https://doi.org/10.1002/2015gl066882>

960 Lee, J.-J., & Bruhn, R. L. (1996). Structural anisotropy of normal fault surfaces. *Journal of*
961 *Structural Geology*, 18(8), 1043–1059. [https://doi.org/10.1016/0191-8141\(96\)00022-3](https://doi.org/10.1016/0191-8141(96)00022-3)

962 Lee, Y.-J. (1991). *Slickenside Petrography: slip-Sense Indicators and Classification* (Master of
963 Sciences). (W. Means, Ed.). State University of New York at Albany. Retrieved from
964 <http://www.atmos.albany.edu/geology/theses/leeyjmstxt.pdf>

965 Lin, A. (2001). S–C fabrics developed in cataclastic rocks from the Nojima fault zone, Japan and
966 their implications for tectonic history. *Journal of Structural Geology*, 23(6), 1167–1178.
967 [https://doi.org/10.1016/S0191-8141\(00\)00171-1](https://doi.org/10.1016/S0191-8141(00)00171-1)

968 Lin, S., & Williams, P. F. (1992). The origin of ridge-in-groove slickenside striae and associated
969 steps in an S-C mylonite. *Journal of Structural Geology*, 14(3), 315–321.
970 [https://doi.org/10.1016/0191-8141\(92\)90089-F](https://doi.org/10.1016/0191-8141(92)90089-F)

971 Lin, S., Jiang, D., & Williams, P. F. (2007). Importance of differentiating ductile slickenside
972 striations from stretching lineations and variation of shear direction across a high-strain
973 zone. *Journal of Structural Geology*, 29(5), 850–862.
974 <https://doi.org/10.1016/j.jsg.2006.12.006>

975 Lyell, S. C. (Ed.). (1871). Chapter XXXVI. Mineral Veins. In *The student's elements of geology*.
976 (pp. 589–602). Thomas Telford Publishing. <https://doi.org/10.1680/tseog.52581.0036>

977 Macklin, C., Kaneko, Y., & Kears, J. (2021). Coseismic slickenlines record the emergence of
978 multiple rupture fronts during a surface-breaking earthquake. *Tectonophysics*, *808*,
979 228834. <https://doi.org/10.1016/j.tecto.2021.228834>

980 Magloughlin, J. F., & Spray, J. G. (1992). Frictional melting processes and products in
981 geological materials: introduction and discussion. *Tectonophysics*, *204*(3), 197–204.
982 [https://doi.org/10.1016/0040-1951\(92\)90307-R](https://doi.org/10.1016/0040-1951(92)90307-R)

983 Mandelbrot, B. B. (1985). Self-Affine Fractals and Fractal Dimension. *Physica Scripta*, *32*(4),
984 257. <https://doi.org/10.1088/0031-8949/32/4/001>

985 Marti, S., Stünitz, H., Heilbronner, R., & Plümper, O. (2020). Amorphous material in
986 experimentally deformed mafic rock and its temperature dependence: Implications for
987 fault rheology during aseismic creep and seismic rupture. *Journal of Structural Geology*,
988 *138*, 104081. <https://doi.org/10.1016/j.jsg.2020.104081>

989 McCool, J. I. (1992). Non-Gaussian effects in microcontact. *International Journal of Machine*
990 *Tools & Manufacture*, *32*(1), 115–123. [https://doi.org/10.1016/0890-6955\(92\)90068-R](https://doi.org/10.1016/0890-6955(92)90068-R)

991 Milanese, E., Brink, T., Aghababaei, R., & Molinari, J.-F. (2019). Emergence of self-affine
992 surfaces during adhesive wear. *Nature Communications*, *10*(1), 1116.
993 <https://doi.org/10.1038/s41467-019-09127-8>

994 Nakamura, N., & Nagahama, H. (2002). Tribochemical wearing in S-C mylonites and its
995 implication to lithosphere stress level. *Earth, Planets and Space*, *54*(11), 1103–1108.
996 <https://doi.org/10.1186/bf03353309>

997 Nielsen, S., Mosca, P., Giberti, G., Di Toro, G., Hirose, T., & Shimamoto, T. (2010). On the

998 transient behavior of frictional melt during seismic slip. *Journal of Geophysical*
999 *Research*, 115(B10). <https://doi.org/10.1029/2009jb007020>

1000 Ohl, M., Plümper, O., Chatzaras, V., Wallis, D., Vollmer, C., & Drury, M. (2020). Mechanisms
1001 of fault mirror formation and fault healing in carbonate rocks. *Earth and Planetary*
1002 *Science Letters*, 530, 115886. <https://doi.org/10.1016/j.epsl.2019.115886>

1003 Ortega-Arroyo, D. (2017). *The Rock Record of Seismic Nucleation and Dynamic Weakening:*
1004 *Case Studies from the Whipple Mountains Detachment Fault, Eastern California.*
1005 University of Texas at Austin.

1006 Otsubo, M., Shigematsu, N., Imanishi, K., Ando, R., Takahashi, M., & Azuma, T. (2013).
1007 Temporal slip change based on curved slickenlines on fault scarps along Itozawa fault
1008 caused by 2011 Iwaki earthquake, northeast Japan. *Tectonophysics*, 608, 970–979.
1009 <https://doi.org/10.1016/j.tecto.2013.07.022>

1010 Passchier, C. W., & Trouw, R. A. J. (2005). *Microtectonics*. Springer, Berlin, Heidelberg.
1011 <https://doi.org/10.1007/3-540-29359-0>

1012 Pec, M., & Al Nasser, S. (2021). Formation of nanocrystalline and amorphous materials causes
1013 parallel brittle-viscous flow of crustal rocks: Experiments on quartz-feldspar aggregates.
1014 *Journal of Geophysical Research*, [Solid Earth], 126(5).
1015 <https://doi.org/10.1029/2020jb021262>

1016 Pec, M., Stünitz, H., Heilbronner, R., Drury, M., & de Capitani, C. (2012). Origin of
1017 pseudotachylites in slow creep experiments. *Earth and Planetary Science Letters*, 355–
1018 356, 299–310. <https://doi.org/10.1016/j.epsl.2012.09.004>

1019 Pec, M., Stünitz, H., Heilbronner, R., & Drury, M. (2016). Semi-brittle flow of granitoid fault
1020 rocks in experiments. *Journal of Geophysical Research*, [Solid Earth], 121(3), 1677–

- 1021 1705. <https://doi.org/10.1002/2015jb012513>
- 1022 Petit, J. P. (1987). Criteria for the sense of movement on fault surfaces in brittle rocks. *Journal of*
1023 *Structural Geology*, 9(5), 597–608. [https://doi.org/10.1016/0191-8141\(87\)90145-3](https://doi.org/10.1016/0191-8141(87)90145-3)
- 1024 Power, W. L., & Tullis, T. E. (1989). The relationship between slickenside surfaces in fine-
1025 grained quartz and the seismic cycle. *Journal of Structural Geology*, 11(7), 879–893.
1026 [https://doi.org/10.1016/0191-8141\(89\)90105-3](https://doi.org/10.1016/0191-8141(89)90105-3)
- 1027 Power, W. L., Tullis, T. E., Brown, S. R., Boitnott, G. N., & Scholz, C. H. (1987). Roughness of
1028 natural fault surfaces. *Geophysical Research Letters*, 14(1), 29–32.
1029 <https://doi.org/10.1029/gl014i001p00029>
- 1030 Ranganathan, M., Minchew, B., Meyer, C. R., & Pec, M. (2021, July 29). *Deformational-energy*
1031 *partitioning in glacier shear zones*. *Earth and Space Science Open Archive*. Earth and
1032 Space Science Open Archive. <https://doi.org/10.1002/essoar.10507633.1>
- 1033 Renard, F., Mair, K., & Gundersen, O. (2012). Surface roughness evolution on experimentally
1034 simulated faults. *Journal of Structural Geology*, 45, 101–112.
1035 <https://doi.org/10.1016/j.jsg.2012.03.009>
- 1036 Romeis, S., Schmidt, J., & Peukert, W. (2016). Mechanochemical aspects in wet stirred media
1037 milling. *International Journal of Mineral Processing*, 156, 24–31.
1038 <https://doi.org/10.1016/j.minpro.2016.05.018>
- 1039 Rosakis, P., Rosakis, A. J., Ravichandran, G., & Hodowany, J. (2000). A thermodynamic
1040 internal variable model for the partition of plastic work into heat and stored energy in
1041 metals. *Journal of the Mechanics and Physics of Solids*, 48(3), 581–607.
1042 [https://doi.org/10.1016/S0022-5096\(99\)00048-4](https://doi.org/10.1016/S0022-5096(99)00048-4)
- 1043 Rosas-Elguera, J., Ferrari, L., Garduño-Monroy, V. H., & Urrutia-Fucugauchi, J. (1996).

1044 Continental boundaries of the Jalisco block and their influence in the Pliocene-
1045 Quaternary kinematics of western Mexico. *Geology*, 24(10), 921–924.
1046 [https://doi.org/10.1130/0091-7613\(1996\)024<0921:CBOTJB>2.3.CO;2](https://doi.org/10.1130/0091-7613(1996)024<0921:CBOTJB>2.3.CO;2)

1047 Rowe, C. D., & Griffith, W. A. (2015). Do faults preserve a record of seismic slip: A second
1048 opinion. *Journal of Structural Geology*, 78, 1–26.
1049 <https://doi.org/10.1016/j.jsg.2015.06.006>

1050 Rowe, C. D., Ross, C., Swanson, M. T., Pollock, S., Backeberg, N. R., Barshi, N. A., et al.
1051 (2018). Geometric complexity of earthquake rupture surfaces preserved in
1052 pseudotachylyte networks. *Journal of Geophysical Research, [Solid Earth]*, 123(9),
1053 7998–8015. <https://doi.org/10.1029/2018jb016192>

1054 Rowe, C. D., Lamothe, K., Rempe, M., Andrews, M., Mitchell, T. M., Di Toro, G., et al. (2019).
1055 Earthquake lubrication and healing explained by amorphous nanosilica. *Nature*
1056 *Communications*, 10(1), 320. <https://doi.org/10.1038/s41467-018-08238-y>

1057 Sagy, A., & Lyakhovsky, V. (2019). Stress patterns and failure around rough interlocked fault
1058 surface. *Journal of Geophysical Research, [Solid Earth]*, 124(7), 7138–7154.
1059 <https://doi.org/10.1029/2018jb017006>

1060 Sagy, A., Brodsky, E. E., & Axen, G. J. (2007). Evolution of fault-surface roughness with slip.
1061 *Geology*, 35(3), 283–286. <https://doi.org/10.1130/G23235A.1>

1062 Scholz, C. H. (2019). *The Mechanics of Earthquakes and Faulting* (3rd ed.). Cambridge:
1063 Cambridge University Press. <https://doi.org/10.1017/9781316681473>

1064 Sedláček, M., Podgornik, B., & Vižintin, J. (2012). Correlation between standard roughness
1065 parameters skewness and kurtosis and tribological behaviour of contact surfaces.
1066 *Tribology International*, 48, 102–112. <https://doi.org/10.1016/j.triboint.2011.11.008>

- 1067 Shervais, K. A. H., & Kirkpatrick, J. D. (2016). Smoothing and re-roughening processes: The
1068 geometric evolution of a single fault zone. *Journal of Structural Geology*, *91*, 130–143.
1069 <https://doi.org/10.1016/j.jsg.2016.09.004>
- 1070 Siman-Tov, S., Aharonov, E., Sagy, A., & Emmanuel, S. (2013). Nanograins form carbonate
1071 fault mirrors. *Geology*, *41*(6), 703–706. <https://doi.org/10.1130/G34087.1>
- 1072 Siman-Tov, S., Aharonov, E., Boneh, Y., & Reches, Z. (2015). Fault mirrors along carbonate
1073 faults: Formation and destruction during shear experiments. *Earth and Planetary Science
1074 Letters*, *430*, 367–376. <https://doi.org/10.1016/j.epsl.2015.08.031>
- 1075 Spray, J. G. (1989). Slickenside formation by surface melting during the mechanical excavation
1076 of rock. *Journal of Structural Geology*, *11*(7), 895–905. [https://doi.org/10.1016/0191-
1077 8141\(89\)90106-5](https://doi.org/10.1016/0191-8141(89)90106-5)
- 1078 Spray, J. G. (1992). A physical basis for the frictional melting of some rock-forming minerals.
1079 *Tectonophysics*, *204*(3), 205–221. [https://doi.org/10.1016/0040-1951\(92\)90308-S](https://doi.org/10.1016/0040-1951(92)90308-S)
- 1080 Sun, H., & Pec, M. (2021). Nanometric flow and earthquake instability. *Nature Communications*,
1081 *12*(1), 6779. <https://doi.org/10.1038/s41467-021-26996-0>
- 1082 Swanson, M. T. (1988). Pseudotachylyte-bearing strike-slip duplex structures in the Fort Foster
1083 Brittle Zone, S. Maine. *Journal of Structural Geology*, *10*(8), 813–828.
1084 [https://doi.org/10.1016/0191-8141\(88\)90097-1](https://doi.org/10.1016/0191-8141(88)90097-1)
- 1085 Tal, Y., Goebel, T., & Avouac, J.-P. (2020). Experimental and modeling study of the effect of
1086 fault roughness on dynamic frictional sliding. *Earth and Planetary Science Letters*,
1087 *536*(116133), 116133. <https://doi.org/10.1016/j.epsl.2020.116133>
- 1088 Tayebi, N., & Polycarpou, A. A. (2004). Modeling the effect of skewness and kurtosis on the
1089 static friction coefficient of rough surfaces. *Tribology International*, *37*(6), 491–505.

1090 <https://doi.org/10.1016/j.triboint.2003.11.010>

1091 Taylor, M. P., Ault, A. K., Odlum, M. L., & Newell, D. L. (2021). Shallow rupture propagation
1092 of Pleistocene earthquakes along the hurricane fault, UT, revealed by hematite (U-Th)/he
1093 thermochronometry and textures. *Geophysical Research Letters*, 48(17).
1094 <https://doi.org/10.1029/2021gl094379>

1095 Thom, C. A., Brodsky, E. E., Carpick, R. W., Pharr, G. M., Oliver, W. C., & Goldsby, D. L.
1096 (2017). Nanoscale roughness of natural fault surfaces controlled by scale-dependent yield
1097 strength. *Geophysical Research Letters*, 44(18), 9299–9307.
1098 <https://doi.org/10.1002/2017gl074663>

1099 Tikoff, B., Chatzaras, V., Newman, J., & Roberts, N. M. (2019). Big data in microstructure
1100 analysis: Building a universal orientation system for thin sections. *Journal of Structural*
1101 *Geology*, 125, 226–234. <https://doi.org/10.1016/j.jsg.2018.09.019>

1102 Tisato, N., Di Toro, G., De Rossi, N., Quaresimin, M., & Candela, T. (2012). Experimental
1103 investigation of flash weakening in limestone. *Journal of Structural Geology*, 38, 183–
1104 199. <https://doi.org/10.1016/j.jsg.2011.11.017>

1105 Tomota, T., Kondoh, Y., & Ohmori, T. (2019). Modeling Solid Contact between Smooth and
1106 Rough Surfaces with Non-Gaussian Distributions. *Tribology Transactions*, 62(4), 580–
1107 591. <https://doi.org/10.1080/10402004.2019.1573341>

1108 Torabi, A., Ellingsen, T. S. S., Johannessen, M. U., Alaei, B., Rotevatn, A., & Chiarella, D.
1109 (2020). Fault zone architecture and its scaling laws: where does the damage zone start
1110 and stop? *Geological Society, London, Special Publications*, 496(1), 99–124.
1111 <https://doi.org/10.1144/SP496-2018-151>

1112 Torabi, A., Balsamo, F., Nogueira, F. C. C., Vasconcelos, D. L., Silva, A. C. E., Bezerra, F. H.

1113 R., & Souza, J. A. B. (2021). Variation of thickness, internal structure and petrophysical
1114 properties in a deformation band fault zone in siliciclastic rocks. *Marine and Petroleum*
1115 *Geology*, 133, 105297. <https://doi.org/10.1016/j.marpetgeo.2021.105297>

1116 Toy, V. G., Niemeijer, A., Renard, F., Morales, L., & Wirth, R. (2017). Striation and slickenline
1117 development on quartz fault surfaces at crustal conditions: Origin and effect on friction.
1118 *Journal of Geophysical Research, [Solid Earth]*, 122(5), 3497–3512.
1119 <https://doi.org/10.1002/2016jb013498>

1120 Tsai, V. C., & Hirth, G. (2020). Elastic impact consequences for high-frequency earthquake
1121 ground motion. *Geophysical Research Letters*, 47(5).
1122 <https://doi.org/10.1029/2019gl086302>

1123 Tsai, V. C., Hirth, G., Trugman, D. T., & Chu, S. X. (2021). Impact versus frictional earthquake
1124 models for high-frequency radiation in complex fault zones. *Journal of Geophysical*
1125 *Research, [Solid Earth]*, 126(8). <https://doi.org/10.1029/2021jb022313>

1126 Ulrich, T., Gabriel, A.-A., Ampuero, J.-P., & Xu, W. (2019). Dynamic viability of the 2016 Mw
1127 7.8 Kaikōura earthquake cascade on weak crustal faults. *Nature Communications*, 10(1),
1128 1213. <https://doi.org/10.1038/s41467-019-09125-w>

1129 Verberne, B. A., Plümper, O., de Winter, D. A. M., & Spiers, C. J. (2014). Rock mechanics.
1130 Superplastic nanofibrous slip zones control seismogenic fault friction. *Science*,
1131 346(6215), 1342–1344. <https://doi.org/10.1126/science.1259003>

1132 Verberne, B. A., Plümper, O., & Spiers, C. J. (2019). Nanocrystalline Principal Slip Zones and
1133 Their Role in Controlling Crustal Fault Rheology. *Minerals*, 9(6), 328.
1134 <https://doi.org/10.3390/min9060328>

1135 Viat, A., Guillonneau, G., Fouvry, S., Kermouche, G., Sao Joao, S., Wehrs, J., et al. (2017).

1136 Brittle to ductile transition of tribomaterial in relation to wear response at high
1137 temperatures. *Wear: An International Journal on the Science and Technology of Friction*
1138 *Lubrication and Wear*, 392–393, 60–68. <https://doi.org/10.1016/j.wear.2017.09.015>

1139 Viti, C., Brogi, A., Liotta, D., Mugnaioli, E., Spiess, R., Dini, A., et al. (2016). Seismic slip
1140 recorded in tourmaline fault mirrors from Elba Island (Italy). *Journal of Structural*
1141 *Geology*, 86, 1–12. <https://doi.org/10.1016/j.jsg.2016.02.013>

1142 Wang, M., Chen, Y.-F., Ma, G.-W., Zhou, J.-Q., & Zhou, C.-B. (2016). Influence of surface
1143 roughness on nonlinear flow behaviors in 3D self-affine rough fractures: Lattice
1144 Boltzmann simulations. *Advances in Water Resources*, 96, 373–388.
1145 <https://doi.org/10.1016/j.advwatres.2016.08.006>

1146 Wang, W.-Z., Chen, H., Hu, Y.-Z., & Wang, H. (2006). Effect of surface roughness parameters
1147 on mixed lubrication characteristics. *Tribology International*, 39(6), 522–527.
1148 <https://doi.org/10.1016/j.triboint.2005.03.018>

1149 Will, T. M., & Wilson, C. J. L. (1989). Experimentally produced slickenside lineations in
1150 pyrophyllitic clay. *Journal of Structural Geology*, 11(6), 657–667.
1151 [https://doi.org/10.1016/0191-8141\(89\)90002-3](https://doi.org/10.1016/0191-8141(89)90002-3)

1152 Wilson, B., Dewers, T., Reches, Z., & Brune, J. (2005). Particle size and energetics of gouge
1153 from earthquake rupture zones. *Nature*, 434(7034), 749–752.
1154 <https://doi.org/10.1038/nature03433>

1155 Wilson, C. J. L., & Will, T. M. (1990). Slickenside lineations due to ductile processes.
1156 *Geological Society, London, Special Publications*, 54(1), 455–460.
1157 <https://doi.org/10.1144/GSL.SP.1990.054.01.41>

1158 Yan, X.-L., Wang, X.-L., & Zhang, Y.-Y. (2014). Influence of Roughness Parameters Skewness

1159 and Kurtosis on Fatigue Life Under Mixed Elastohydrodynamic Lubrication Point
1160 Contacts. *Journal of Tribology*, 136(3). <https://doi.org/10.1115/1.4027480>

1161 Zhang, S., Wang, W., & Zhao, Z. (2014). The effect of surface roughness characteristics on the
1162 elastic–plastic contact performance. *Tribology International*, 79, 59–73.
1163 <https://doi.org/10.1016/j.triboint.2014.05.016>

1164 Zhang, Y. S., Zhang, L. C., Niu, H. Z., Bai, X. F., Yu, S., Ma, X. Q., & Yu, Z. T. (2014).
1165 Deformation twinning and localized amorphization in nanocrystalline tantalum induced
1166 by sliding friction. *Materials Letters*, 127, 4–7.
1167 <https://doi.org/10.1016/j.matlet.2014.04.079>

1168 Zhao, S., Hahn, E. N., Kad, B., Remington, B. A., Wehrenberg, C. E., Bringa, E. M., & Meyers,
1169 M. A. (2016). Amorphization and nanocrystallization of silicon under shock
1170 compression. *Acta Materialia*, 103, 519–533.
1171 <https://doi.org/10.1016/j.actamat.2015.09.022>